

AD-A129 432

JOURNAL OF ENGINEERING THERMOPHYSICS (SELECTED
ARTICLES)(U) FOREIGN TECHNOLOGY DIV WRIGHT-PATTERSON
AFB OH C TS'UI ET AL. 20 MAY 83 FTD-ID(RS)T-0377-83

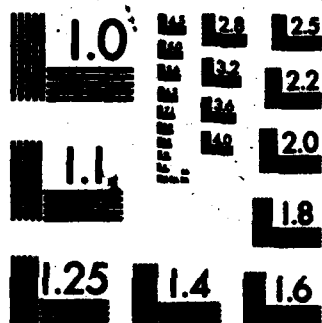
17

UNCLASSIFIED

F/G 21/5

NL

END
DATE
FILMED
DTIC



MICROCOPY RESOLUTION TEST CHART
NATIONAL BUREAU OF STANDARDS-1963-A

AD A129432

FTD-ID(RS)T-0377-83

FOREIGN TECHNOLOGY DIVISION



JOURNAL OF ENGINEERING THERMOPHYSICS

(Selected Articles)



DTIC
ELECTE
JUN 17 1983
S D

Approved for public release;
distribution unlimited.

DTIC FILE COPY

88 06 16 08

Accession For	
NTIS GRA&I	<input checked="" type="checkbox"/>
DTIC TAB	<input type="checkbox"/>
Unannounced	<input type="checkbox"/>
Justification	
By _____	
Distribution/	
Availability Codes	
Dist	Avail and/or Special
A	



FTD -ID(RS)T-0377-83

EDITED TRANSLATION

FTD-ID(RS)T-0377-83

20 May 1983

MICROFICHE NR: FTD-83-C-000669

JOURNAL OF ENGINEERING THERMOPHYSICS (Selected Articles)

English pages: 85

Source: Gongcheng Rewuli Xuebao, Vol. 2, Nr. 2, 1981,
pp. 106-110; 121-144; 160-172; 185-187

Country of origin: China

Translated by: SCITRAN

F33657-81-D-0263

Requester: FTD/TQTA

Approved for public release; distribution unlimited.

THIS TRANSLATION IS A RENDITION OF THE ORIGINAL FOREIGN TEXT WITHOUT ANY ANALYTICAL OR EDITORIAL COMMENT. STATEMENTS OR THEORIES ADVOCATED OR IMPLIED ARE THOSE OF THE SOURCE AND DO NOT NECESSARILY REFLECT THE POSITION OR OPINION OF THE FOREIGN TECHNOLOGY DIVISION.

PREPARED BY:

TRANSLATION DIVISION
FOREIGN TECHNOLOGY DIVISION
WP.AFB, OHIO.

FTD -ID(RS)T-0377-83

Date 20 May 19 83

Table of Contents

Graphics Disclaimer	ii
Approximate Analytical Solution for the Optimum Cycle Parameters of Turbofan Engines with Equal Total Pressure Mixing Exhaust, by <u>Ts'ui Chi-ya</u>	1
Application of the Time-Dependent Finite-Volume Method to the Calculation of Transonic Cascade Flow Field, by <u>Chou Hsin-hai</u> , <u>Liu Sung-ling</u> , <u>Fan Fei-ta</u> , <u>Chu Fang-yuan</u>	9
A Surge Test of a Twin-Shaft Turbojet Engine on Ground Test Bed, by <u>Chiang Feng</u>	26
Effect of Blade Stagger Angle on Performance of a Transonic Compressor with Low Hub-Tip Ratio, by <u>Chao Shin-ch'un</u>	41
The Stage Matching Problem and Optimization Analysis of Multi-Stage Turbines, by <u>Ke Man-ch'u</u>	57
Investigation of the Rotor Wake in a Single Stage Axial Flow Compressor, by <u>Chang Wei-te</u> , <u>Lin Ch'1 hsun</u>	64
Thermal Conductivity Measurement of Materials During Ablation-- A Treatment on the Moving Boundary Problem, by <u>Chou Pen-lien</u> , <u>Wei Chen</u> , <u>Lin Chun-heng</u>	69
A Method for Measuring Multiple Thermalphysical Properties of Metallic Materials at High Temperature, by <u>Yao Lung-ch'in</u> , <u>He Lu-ping</u> , <u>Hao-Yu-ts'ai</u> , <u>Kuo-I'ling</u>	81

GRAPHICS DISCLAIMER

All figures, graphics, tables, equations, etc. merged into this translation were extracted from the best quality copy available.

APPROXIMATE ANALYTICAL SOLUTION FOR THE OPTIMUM CYCLE PARAMETERS OF TURBOFAN ENGINES WITH EQUAL TOTAL PRESSURE MIXING EXHAUST*

Ts'ui Chi-ya

(Beijing Institute of Aeronautics and Astronautics)

ABSTRACT

This paper sets forth an approximate analytical solution for the optimum cycle parameters of turbofan engines with equal total pressure mixing exhaust. With a given bypass ratio, three respective optimum compressor pressure ratios for thrust, s.f.c. and fan pressure ratio may be determined, the last one meaning both thrust and s.f.c. optimum when reheating.

I. FOREWORD

/106*

Although some research has been done on the optimum cycle parameters of turbofan engines with equal total pressure mixing exhaust, no analytical solution has yet been found for this problem. By grouping sets of constants together, we have, for the first time, set forth an approximate analytical solution for turbofan engines with equal total pressure mixing under the condition of a given bypass ratio.

*This article was read during the Third National Meeting of the Engineering Thermophysics Conference held in Kueilin in April, 1980.

**Numbers in the margin indicate pagination of foreign text.

II. METHOD AND RESULTS

From Figure 1, which gives the working process of the turbofan engine with equal total pressure mixing exhaust, the conversion of internal energy to external energy is given by

$$B(i_2^* - i_1^*) = v_f(1 + g_{rr})(i_2^* - i_1^*)$$

Employing basic thermodynamic relations, this can be written as

$$B = \frac{v_f(1 + g_{rr}) \left[i_2^* - \frac{c_{pr} T_1^* (p_2^*/p_1^*)^{\frac{\gamma_r - 1}{\gamma_r}} - 1 \right] - \frac{c_{pr}}{c_{pr}} \left[1 - \left(\frac{p_2^*}{p_1^*} \right)^{\frac{\gamma_r - 1}{\gamma_r}} \right] i_1^*}{c_{pr} T_1^* (p_2^*/p_1^*)^{\frac{\gamma_r - 1}{\gamma_r}} - 1} \quad (a)$$

where v_f and v_k are coefficients of turbofan engine air cooling. The subscripts, f, k, and r refer to the fan, the compressor and the burning gas, and c_{pr} is the average specific heat of the burning gas from 0°K to T_1^* .

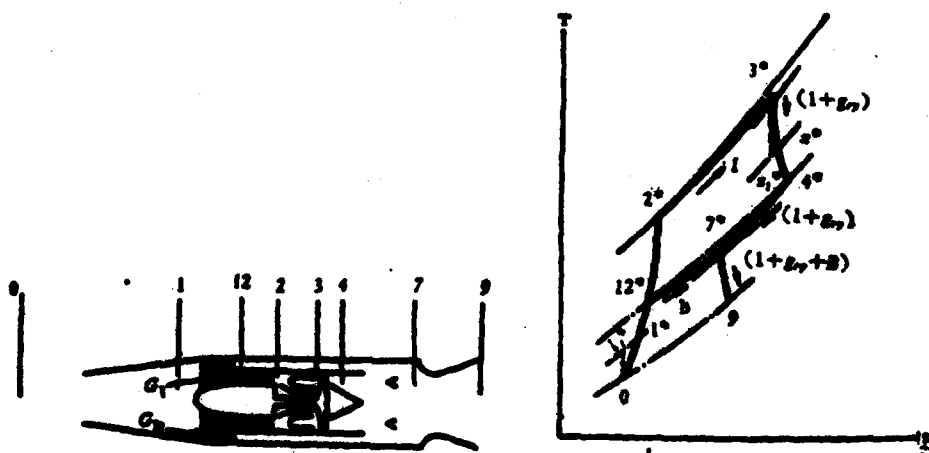


Figure 1. Working process of the turbofan engine with equal total pressure mixing.

Making use of the relation of equal total pressure mixing, $p_{12}^* = p_1^*$, we obtain:

$$\frac{\pi_2^{k-1}}{\pi_1^{k-1}} + \frac{F_1}{BF_2} \frac{F_2 - \pi_2^{k-1}}{\pi_2^{k-1}(F_2 - \pi_2^{k-1})} \pi_2^{k-1} - \left[1 + \frac{F_1}{B} (F_2 - \pi_2^{k-1}) \right] - f(\pi_2^*, \pi_2^*) = 0 \quad (1)$$

In the above equation,

$$\begin{aligned} \text{式中 } F_1 &= v_f \eta_f^* \eta_f^* c_p c_{p2} / c_{p2} c_p v_k \eta_k^*; F_2 = [i_2^* v_k (1 + g_{r2}) \eta_k^* / c_{p2} T_1^*] + 1; \\ F_3 &= c_{p2} T_1^* \sigma_r^{k-1} / c_p T_2^* \gamma_k (1 + g_{r2}) \eta_k^* \eta_f^* \\ F_4 &= [c_p T_2^* v_k (1 + g_{r2}) \eta_k^* \eta_f^* / c_{p2} T_1^*] + 1. \end{aligned}$$

(σ_r is the coefficient of total pressure of the combustion chamber.)

After each constant, F has been found for given efficiency and coefficients, one can determine from

$$\frac{d\pi_2^*}{d\pi_1^*} = - \frac{\partial f}{\partial \pi_1^*} / \frac{\partial f}{\partial \pi_2^*} = 0 \quad (2)$$

the compressor pressure ratio (π_k^*) _{π_f^*} that maximizes the fan pressure ratio.

The unit thrust of the internal flow is

$$R/G_1 = (1 + g_{r2} + B) c_{p2} / g - (1 + B) V / g$$

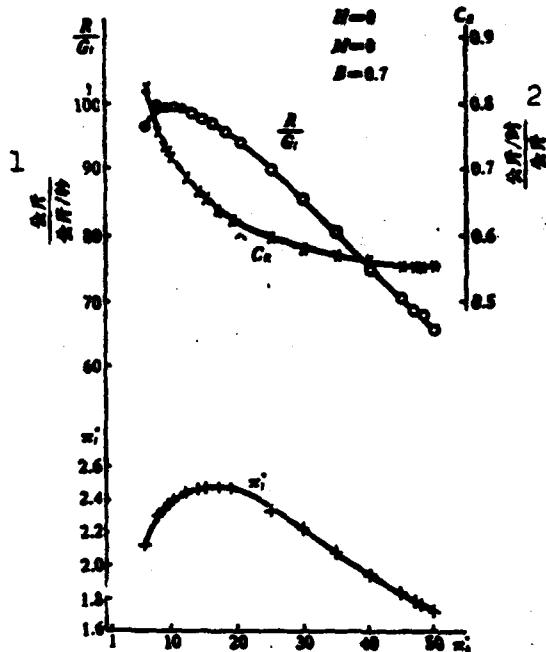
where

$$V = M \sqrt{k_g R T_0} = \sqrt{2g} j_{i0} \sqrt{(k-1)/2M};$$

Assuming here that $v_f = 1$ approximately, one has

$$c_p = \sqrt{2g} j_{i0} \left\{ \eta_f \frac{c_{p2}}{c_p} \left[\frac{(1 + g_{r2}) \left[\frac{\pi_2^*}{\pi_1^*} - \frac{c_{p2} T_1^* (\pi_2^{k-1} - 1)}{(1 + g_{r2}) c_p \eta_k^*} \right] + B \frac{\pi_2^*}{\pi_1^*}}{(1 + g_{r2} + B)} \right] \right. \\ \left. \cdot \left[1 - \left(\frac{1}{(1 + \eta_k (m-1))^{1-\frac{k-1}{\gamma_k}} \pi_2^* \sigma_r} \right)^{\frac{k-1}{\gamma_k}} \right] \right\}$$

(In the above equation, C_{p07} is the average specific heat of the burning gas from 0°K to T_7^* ; σ_h is the coefficient of the total pressure of the mixer; $m=1+(k-1)M^2/2$ is the ratio of pressure to temperature increase during flight.)



($T_7^* = 1356\text{K}$, $\eta_7^* = 0.778$, $\eta_7^* = 0.841$, $\eta_7^* = 0.925$, $\eta_{pA} = 0.9725$, $H = 10300$, $g = 0.97$, $v = 0.91$, $g_{rj} = 0.01638$, $v_A = 0.9456$, $v_f = 0.97$, $\sigma = 0.96$, $\sigma_A = 0.97$, $C_{pA} = 0.2475$, $k_A = 1.383$, $C_{p1} = 0.2392$, $k_1 = 1.402$, $C_{p2} = 0.284$, $k_2 = 1.317$, $C_{p3} = 0.2525$, $C_{p4} = 0.246$, $c_{p1} = 0.2548$, $k_1^* = 1.368$)

Figure 2. Effect of π_k^* during stay on ground.

Key: 1) $\text{kg}/(\text{kg}/\text{sec})$; 2) $(\text{kg}/\text{hr})/\text{kg}$.

Therefore, the zero-order thrust is

$$\begin{aligned} \bar{R} &= (R/G)g/\sqrt{2gI_0} \\ &= \sqrt{(1 + g_{rj} + B) \eta_{pA} c_{pA} T_7^* / c_{p1} \eta_7^*} \bar{R}_0 - (1 + B) \sqrt{(k-1)/2M} \end{aligned} \quad (b)$$

where

$$\bar{R}_0 = \sqrt{(F_1 - \pi_k^* \frac{k-1}{k}) (1 - A \pi_k^* \frac{k-1}{k})} \quad (3)$$

(In the above equation,

$$(\text{式中 } F_5 = (1 + g_{r2}) \frac{v_{k2}^2}{c_{p2} T_1^2} + B \frac{v_{k1}^2}{c_{p1} T_1^2} + 1$$

$$A_5 = ([1 + \eta_{1k}(m-1)]^{\frac{1}{1-\gamma}} \sigma_2)^{\frac{1-\gamma}{\gamma}}$$

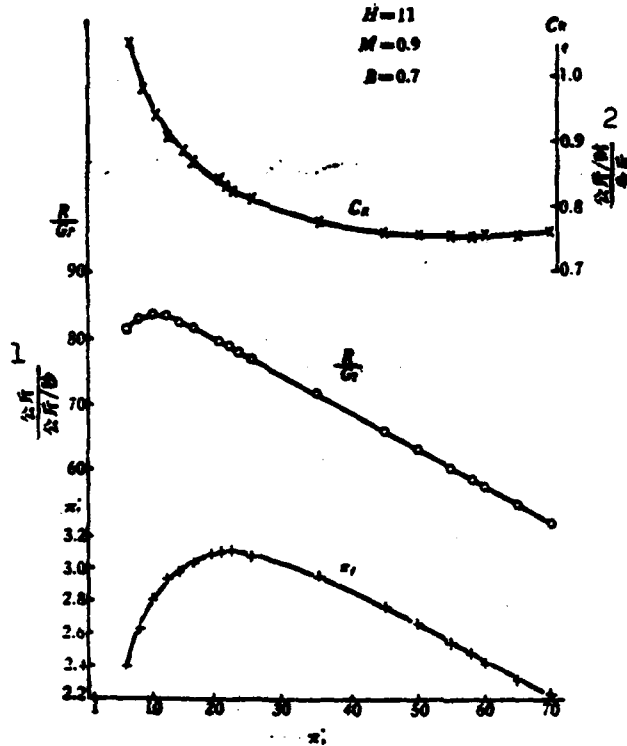


Figure 3. Effect of π_k^* during cruise in the stratosphere.

Key: ($k=1.402$, $\eta_{jk}=0.99$; the rest is the same as in Figure 2).

1) $\text{kg}/(\text{kg}/\text{sec})$; 2) $(\text{kg}/\text{hr})/\text{kg}$.

From

/109

$$\frac{dR_1}{d\pi_k^*} - \frac{\partial R_1}{\partial \pi_k^*} + \frac{\partial R_1}{\partial \pi_k} \frac{d\pi_k}{d\pi_k^*} = 0 \quad (4)$$

one can obtain the compressor ratio (π_k^*) R that maximize the thrusts \hat{R}_0 , \bar{R} and R .

Although in the above derivation the variation with π_k^* of s_{py} in the various constant F is very small compared to 1 and can be neglected, s.f.c. is directly dependent on s_{py} , and obviously must be taken into consideration:

$$C_x = \frac{R_{py} \cdot 3600}{R/G_1} = \frac{i_{3a}^* - i_1^*}{(H_1 - i_1^* T_1^* + i_1^*)} \cdot 3600/R \sqrt{2j_{1a}/g}$$

in which i_{3a}^* is the air enthalpy of T_3^* ; i_1^* is the enthalpy difference for constant temperature combustion [3,4]; v is the coefficient of air cooling in the combustion chamber. As i_1^* is very much less than the other terms in the denominator, it can be omitted and we have

$$C_x = 3600 \sqrt{\frac{R}{2j_{1a}}} \frac{c_{pa} T_1^*}{(H_1 - i_1^* T_1^*)} \frac{[(i_{3a}^* - i_1^*)^2 / c_{pa} T_1^* + 1]}{R} = \frac{H_2 - i_1^* T_1^*}{H_1 H_2 - H_1} \quad (c)$$

$$= \frac{H_2 - i_1^* T_1^*}{H_1 H_2 - H_1} \quad (\text{式中 } H_1 = F_1/H_1; H_2 = F_2/H_1) \quad (5)$$

(In this equation, $H_4 = F_7/H_1$; $H_3 = F_6/H_1$)

From the following equation we can find the compressor compression ratio $(\pi_k^*)_{C_R}$ that minimizes the s.f.c.:

$$\frac{dC_x}{d\pi_k^*} = \frac{\partial C_x}{\partial \pi_k^*} + \frac{\partial C_x}{\partial \pi_k^*} \frac{d\pi_k^*}{d\pi_k^*} = 0 \quad (6)$$

In the above equation, note that

$$\frac{\partial C_x}{\partial \pi_k^*} = \left(\frac{H_2 - 1}{H_1 \pi_k^*} + H_1 C_x \frac{1}{\pi_k^*} \frac{\partial \pi_k^*}{\partial \pi_k^*} \right) / (H_1 - H_1 H_2);$$

$$\frac{\partial C_x}{\partial \pi_k^*} = H_1 C_x \frac{1}{\pi_k^*} \frac{\partial \pi_k^*}{\partial \pi_k^*} / (H_1 - H_1 H_2).$$

Figures 2 and 3 are examples of the computation. After we calculated the values of c_p , k for each section using $\pi_k^* = 19.05$ ($\pi_f^* = 2.76$) during a stay on the ground, these values were taken to be approximately constant when π_k^* varied. Each figure represents the results obtained with the help of a microcomputer. (The quantities in parentheses are results obtained by employing the Felix 256 computer.)

	$(\pi_k^*)_R$	$(\pi_k^*)_{of}$	$(\pi_k^*)_{CR}$
During stay on ground:	9.9(10.41)	17(15.25)	47(37.26)
During cruise in the stratosphere:	9.95(10.68)	22(21.99)	58.55(46.97)

The fan pressure ratio that optimizes thrust and s.f.c. is optimum fan pressure ratio. This means that during reheat, thrust is optimum, and it is easy to prove that at the same time s.f.c. is optimum.

III. CONCLUSION

The solutions obtained by setting the specific heat and the value of k constant for each separate part are fairly satisfactory. However, further research needs to be done to compare these results with the exact solution, and to determine the effect of varying the initial data on the optimum parameters.

Please refer to [5] for the approximate solution for the optimum circulation parameters under the condition of a given compressor compression ratio.

REFERENCES

- [1] Hartmann, A.: Research on the Mixing in Bypass Fan Jet Engine, NASA TT F12562.
- [2] Kolodochkin, V.P.: Air Jet Engine of a Supersonic Plane under Various Flight Conditions, Mashgiz, Moscow, 1975, 103.
- [3] Markov, N.I., Bakulev, V.I.: Computation of the High-Speed Characteristics of Turboengine, Oborongiz, Moscow, 1960.
- [4] Fan Tso-ming: Tables of Enthalpy and Applications, Kuo Fang, Kung Ye Publishing House, Peiching (1976).
- [5] Tsuei Chi-ya: Title same as this article, Pei Hang Science Research Report BH-B367, Beiching Institute of Aeronautics and Astronautics (1978).

APPLICATION OF THE TIME-DEPENDENT FINITE-VOLUME METHOD
TO THE CALCULATION OF TRANSONIC CASCADE FLOW FIELD

Chou Hsin-hai Liu Sung-ling Fan Fei-ta Chu Fang-yüan
(Northwestern Polytechnical University)

ABSTRACT

Based on analysis of the J.D. Denton scheme, we have adopted the R.W. MacCormack time-split finite-volume method to calculate the transonic cascade flow field, and thus have obtained better agreement with experimental data. The effect of employing local allowable time step size and a refined mesh to increase the rate of convergence is discussed. Several techniques of artificial viscosity are analyzed. The rule of information propagation, after the energy equation is replaced by the relation of constant stagnation enthalpy along the streamline, is examined.

/121

I. FOREWORD

The time-dependent finite-volume method is one of the effective methods for calculating a transonic cascade flow field. We have, in this paper, analyzed two schemes of this method, viz. the Denton scheme^[1] and the MacCormack^[2] scheme^[2]. Our purpose is to find a reliable method for computing in the design of transonic cascades. When using a time-dependent method of solution, an important criterion for the practicality of the method is the rate of convergence. In this paper, we have adopted the refined mesh approach and used local allowable time step size to increase the rate of convergence of the computation. This approach proved to be effective. Furthermore, we have discussed the change in the rule of propagation of information in the flow field and its effect

on the stability of computation, after the energy equation is replaced by the relation of constant stagnation enthalpy along the streamline.

II. BASIC EQUATIONS

The basic equations for a two-dimensional, inviscid, thermally nonconducting, unsteady, unconstant flow are

$$\partial \rho / \partial t + \partial \rho V_x / \partial x + \partial \rho V_y / \partial y = 0 \quad (1)$$

$$\partial V_x / \partial t + V_x \partial V_x / \partial x + V_y \partial V_x / \partial y + \rho^{-1} \partial p / \partial x = 0 \quad (2)$$

$$\partial V_y / \partial t + V_x \partial V_y / \partial x + V_y \partial V_y / \partial y + \rho^{-1} \partial p / \partial y = 0 \quad (3)$$

$$\partial E / \partial t + \partial [V_x (E + p)] / \partial x + \partial [V_y (E + p)] / \partial y = 0 \quad (4)$$

in which ρ is density, V_x and V_y are velocity components along the x and y directions, respectively, p is pressure and E is the total internal energy per unit volume. Equation (4) is an energy equation. If we let H represent the stagnation enthalpy, then when the flow field approaches a steady state, Equation [4] can be rewritten as

$$DH/Dt = 0 \quad (5)$$

i.e., H is constant along the streamline. For the purpose of solving for a steady state flow field, replacing Equation [4] with Equation [5] will give an accurate result with reduced computational work. After Equation [4] is replaced with Equation [5], the set of equations still retains its hyperbolic form. However, the rule of information propagation is changed. Let us now discuss the changes in the region of physical interest associated with the set of equations under this condition. In order to do this, we have studied the direction of the characteristic plane of the set of equations. First, rewrite Equation [5] as

$$t \frac{\partial p}{\partial t} + v_x \frac{\partial p}{\partial x} + v_y \frac{\partial p}{\partial y} - a^2 \left(\frac{\partial p}{\partial t} + v_x \frac{\partial p}{\partial x} + v_y \frac{\partial p}{\partial y} \right) = 0 \quad (6)$$

where k is the insulation index; a is the speed of sound. A linear combination of Equations [1], [2], [3] and [6] gives, with coefficients α_i ($i=1,2,3,4$),

$$\eta_1 \cdot \nabla \rho + \eta_2 \cdot \nabla V_x + \eta_3 \cdot \nabla V_y + \eta_4 \cdot \nabla p = 0 \quad (7)$$

where

$$\begin{aligned} \eta_1 &= (\alpha_1 - a^2 \alpha_4, V_x \alpha_1 - a^2 V_y \alpha_4, V_y \alpha_1 - V_x a^2 \alpha_4) \\ \eta_2 &= (\alpha_1, \rho \alpha_1 + V_x \alpha_2, V_y \alpha_2) \\ \eta_3 &= (\alpha_2, V_x \alpha_2, \rho \alpha_1 + V_y \alpha_3) \\ \eta_4 &= (k \alpha_4, \alpha_2 / \rho + V_x \alpha_4, \alpha_3 / \rho + V_y \alpha_4) \end{aligned}$$

A general hyperbolic equation set possessing three variables can, at most, have one linear combination of the original partial equations such that the related variables can have derivatives taken along the direction of their common plane, which is the characteristic plane. Hence, if we let $\lambda = (\lambda_t, \lambda_x, \lambda_y)$ be the normal vector of the characteristic plane, then

$$\lambda \cdot \eta_i = 0 \quad (i=1, 2, 3, 4) \quad (8)$$

Equation [8] is a set of linear equations associated with α_i . The necessary and sufficient condition for it to have a non-zero solution is

$$\begin{vmatrix} d & 0 & 0 & -a^2 d \\ \rho \lambda_x & d & 0 & 0 \\ \rho \lambda_y & 0 & d & 0 \\ 0 & \lambda_x / \rho & \lambda_y / \rho & (k-1) \lambda_t + d \end{vmatrix} = 0 \quad (9)$$

where $d = \lambda_t + V_x \lambda_x + V_y \lambda_y$.

From Equation [9], the two non-zero solutions for d are given by

$$d = [-(k-1)\lambda \pm \sqrt{(k-1)^2\lambda^2 + 4\sigma^2(\lambda_x^2 + \lambda_y^2)}] / 2$$

Letting $\lambda_x^2 + \lambda_y^2 = 1$, we can derive

$$\lambda_x + V_x \lambda_x + V_y \lambda_y = \frac{k-1}{2k} (\lambda_x V_x + \lambda_y V_y) \pm \frac{\sigma}{\sqrt{k}} \sqrt{1 + \frac{(k-1)^2}{4k} (\lambda_x V_x + \lambda_y V_y)^2} \quad (10)$$

Equation [10] expresses the relationship between the normal vector of the characteristic plane and the flow parameters and determines the rule of propagation of information in the flow field. From Equation [10], one can obtain the region of physical interest on the xy -plane associated with the set of equations containing Equation [5]. This region is limited to within the region prescribed by the following geometrical elliptic equation (See Figure 1):

$$\frac{x^2}{a^2 \{1/k + [M(k-1)/(2k)]^2\}} + \frac{y^2}{a^2/k} = 1 \quad (11)$$

where M is the Mach number. Therefore, we see that after the energy equation is replaced by Equation [5], information is propagated within a characteristic elliptical cone in the three-dimensional coordinate system (x, y, t) . On the other hand, when Equation [4] is used, the information in the flow field is propagated within the characteristic cone that intercepts the xy -plane at a circle whose radius is the speed of light a . Figure 1 gives a comparison of the bases of the elliptical cone and the cone for various given Mach numbers. In this figure, $oo' = \sqrt{V_x^2 + V_y^2}$ represents distance covered per unit time. The largest distance attainable by information propagation in the flow field is

$$o'A_1 = \sqrt{V_1^2 + V_2^2} + a$$

for the characteristic cone

$$o'A_2 = \sqrt{V_1^2 + V_2^2} + a \cdot K(M)$$

for the characteristic elliptic cone

where

$$K(M) = \sqrt{1/k + [M(k-1)/(2k)]^2} - M(k-1)/(2k)$$

The value of the function $K(M)$ is always less than 1. Hence, $o'A_1$ is always greater than $o'A_2$. The above property of the characteristic elliptic cone shows that, since the region of physical interest has been reduced in size, the stability of the difference equations can be expected to improve by replacing Equation [4] by Equation [5], given the condition of using the same difference scheme.

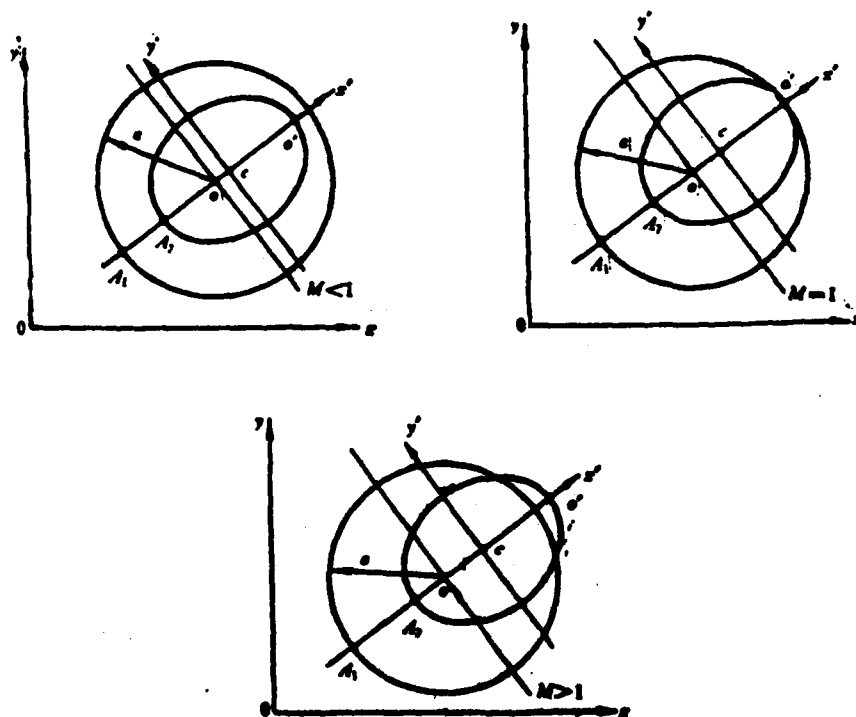


Figure 1.

When finding the solution by the method of finite volume, we employ the integral form of the basic equations. Rewriting Equations [2] and [3] in the form of the equation of conservation, the integral form of the basic equation becomes, for a certain area ΔA ,

$$\frac{\partial}{\partial t} \int_{\Delta A} U dA + \int_s H \cdot \xi ds = 0 \quad (12)$$

where

$$U = \begin{bmatrix} \rho \\ \rho V_x \\ \rho V_y \end{bmatrix}, \quad H = \begin{bmatrix} \rho V_x i_x + \rho V_y i_y \\ (p + \rho V_x^2) i_x + (\rho V_x V_y) i_y \\ (\rho V_x V_y) i_x + (p + \rho V_y^2) i_y \end{bmatrix}$$

ξ is the unit outward normal vector of the perimeter s of the area ΔA ; i_x and i_y are unit vectors parallel to the x and y axes, respectively. Equation [5] can be written as

$$kp / [(k-1)\rho] + (V_x^2 + V_y^2)/2 = \text{constant} \quad (13)$$

Equations [12] and [13] form the basic set of equations from which the solutions can be found.

III. THE MESH SCHEME AND THE FINITE DIFFERENCE SCHEME

The mesh used in Denton's method is shown in Figure 2. It is formed by lines parallel to the y -axis and the lines joining the points of equal divisions along the y direction (simulated streamlines). In Figure 2, ABCD is a unit for computation. Following the basic trend of thought used in the improved Denton scheme as given in [1], we set up the finite difference equations, and calculated a series of transonic cascade flow fields. The results indicate that the fairly good accuracy and fast convergence meet

the demands of engineering computation. However, there is still a definite deviation from data obtained experimentally. Furthermore, even in the absence of shock waves, the total flow pressure on the surface of the object is different from the upstream total pressure, with a difference of $\pm 5\%$. This definitely affects the accuracy of the calculation. In search of a way to improve the computation results, we tried MacCormack's time-split finite-volume scheme. This method has been successfully applied to the solution of problems related to external flows. It possesses a second-order degree of accuracy both in time and space. Moreover, by employing the time-split scheme, it converts the multi-dimensional flow computation into many one-dimensional flow computations, carried out in a definite order, thus increasing the allowable time step size. This scheme allows the choice of any rectangular mesh. In the present computation, we have chosen the same mesh as mentioned above, except with the point of computation (i,j) located in the center of each rectangle. (See EFGH in Figure 2.)

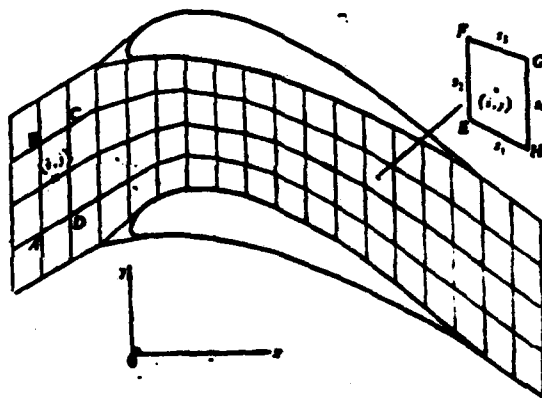


Figure 2.

The time-split finite difference equations for Equation [12] are

$$U_{i,j}^{n+1/2} = U_{i,j}^n - (\Delta t / \Delta A_{i,j}) (H_{i,j}^n \cdot s_1 + H_{i,j-1}^n \cdot s_2) \quad (14)$$

$$U_{i,j}^{n+3/2} = 0.5 [U_{i,j}^n + U_{i,j}^{n+1/2} - (\Delta t / \Delta A_{i,j}) (H_{i,j}^{n+1/2} \cdot s_1 + H_{i,j}^{n+1/2} \cdot s_2)] \quad (15)$$

$$U_{i,j}^{n+1} = U_{i,j}^{n+3/2} - (\Delta t / \Delta A_{i,j}) (H_{i,j}^{n+3/2} \cdot s_1 + H_{i,j+1}^{n+3/2} \cdot s_2) \quad (16)$$

$$U_{i,j}^{n+1} = 0.5 [U_{i,j}^{n+3/2} + U_{i,j}^{n+1} - (\Delta t / \Delta A_{i,j}) (H_{i,j}^{n+3/2} \cdot s_1 + H_{i,j}^{n+3/2} \cdot s_2)] \quad (17)$$

In the above equations, $s_1 = \xi_{i,j}$ ($i=1,2,3,4$); ξ_i is the unit outward normal vector of each side of the mesh unit; s_i is the length of each side of the mesh unit. (See Figure 2.) We can put Equations [14] and [15], Equations [16] and [17], and the operations specified from Equation [14] to Equation [17] in their respective operator form as follows:

$$U_{i,j}^{n+1/2} = L_1(\Delta t) U_{i,j}^n, \quad U_{i,j}^{n+1} = L_2(\Delta t) U_{i,j}^{n+1/2} \\ \text{和 } U_{i,j}^{n+1} = L_2(\Delta t) L_1(\Delta t) U_{i,j}^n.$$

This series of operations has only first order accuracy. To eliminate the effect of the order of operation, one should find the solutions in the order from $U_{i,j}^n$ to $U_{i,j}^{n+2}$, according to the following symmetrical order:

$$U_{i,j}^{n+2} = L_2(\Delta t) L_1(\Delta t) L_2(\Delta t) L_1(\Delta t) U_{i,j}^n.$$

Then, second-order accuracy can be obtained.

When operating at the point (i,j) using the set of equations /125 containing Equation [4], the maximum allowable time step size that ensures stability is

$$\text{for operating on } L_y(\Delta t): \quad \Delta t_{y,i,j} \leq \Delta A_{i,j} / (|q \cdot s_1| + s_1 |s_1|)_{i,j} \quad (18)$$

$$\text{for operating on } L_x(\Delta t): \quad \Delta t_{x,i,j} \leq \Delta A_{i,j} / (|q \cdot s_2| + s_2 |s_2|)_{i,j} \quad (19)$$

where $q = V_x i_x + V_y i_y$. Usually, the smallest values for $\Delta t_{x,i,j}$ and $\Delta t_{y,i,j}$ in the field are taken to be the time step size for the entire field. Considering the non-linearity of the equations,

the actual step size taken is usually smaller than that specified by Equations [18] and [19]. As has been said before, by replacing Equations [4] with [5], one can improve the stability of the difference equations, and adequately increase the time step size.

In the following discussion, the first scheme will be referred to as Method 1, while the second scheme will be referred to as Method 2.

IV. ARTIFICIAL VISCOSITY

Computations indicate that, when we calculated in the cases with stronger shock waves, the "mesh viscosity" inherent in both Method 1 and Method 2 is insufficient. It is therefore necessary to introduce artificial viscosity. We adopted the fourth-order resistance suggested in [4]. For two-dimensional flow it takes the form:

$$(\Delta U_{i,j})_x = c_x \left| \frac{p_{i-1,j} - 2p_{i,j} + p_{i+1,j}}{p_{i-1,j} + 2p_{i,j} + p_{i+1,j}} \right| (U_{i+1,j} - 2U_{i,j} + U_{i-1,j}) \cdot (a_{i,j} + |V_{x,i,j}|) \Delta t / \Delta x \quad (20)$$

$$(\Delta U_{i,j})_y = c_y \left| \frac{p_{i,j-1} - 2p_{i,j} + p_{i,j+1}}{p_{i,j-1} + 2p_{i,j} + p_{i,j+1}} \right| (U_{i,j+1} - 2U_{i,j} + U_{i,j-1}) \cdot (a_{i,j} + |V_{y,i,j}|) \Delta t / \Delta y \quad (21)$$

where U represents the flow parameters (p, pV_x, pV_y), c_x and c_y are selected coefficients, and ΔU is a correction factor for the flow parameters. The error introduced into the difference equations by Equations [20] and [21] is of fourth order, i.e., very minor.

Figure 3 shows the distribution of Mach number as calculated by Method 1 for a one-dimensional contraction-expansion nozzle during excessive expansion. It is clear that the fourth-order resistance has a negligible effect in the smooth region, while

it lowers the peak value of the Mach number appreciably in the vicinity of the shock wave, meanwhile maintaining a good resolution for the parameters. Hence, the fourth-order resistance provides a way for improving the difference scheme when applied to the flow field with fairly strong shock waves. In our computation, we have tried another kind of artificial viscosity that has an even simpler form, namely

$$\bar{U}_{i,j} = U_{i,j} + (U_{i+1,j} + U_{i-1,j} + U_{i,j+1} + U_{i,j-1} - 4U_{i,j})/(\varphi + 4) \quad (22) \quad /126$$

where \bar{U} represents the flow parameters after correction; φ is the coefficient of resistance. When one takes $\varphi \geq 1/\Delta$ (Δ is the smaller of Δx and Δy), Equation [22] will not affect the accuracy of the second-order scheme. While dealing with cascade flows with appreciable shock wave, we have employed this form of resistance, thus ensuring stability of our computation.

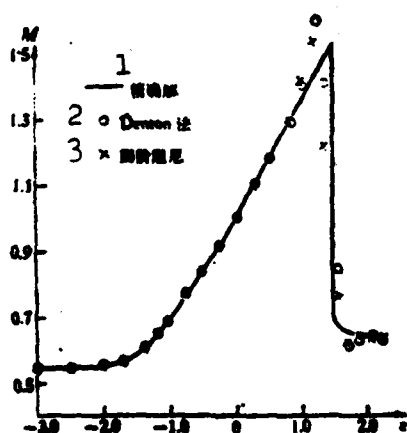


Figure 3.

Key: 1) exact solution; 2) Denton method; 3) fourth-order resistance.

V. EXAMPLES OF COMPUTATION

1. NACA Subsonic Turbine Blade Cascade with 80° Deflection Angle

Figure 4 shows the coefficient of pressure on the surface as computed by means of Method 1 and Method 2 for the blade parameters and flow conditions given in Reference [5] for such a cascade. In this figure, \bar{c} is the relative coordinate along the direction of the chord, and the pressure coefficient $\bar{s} = 2(P_1^* - p)/\rho_1 V_1^2$, where the subscript 1 denotes upstream, and P^* and V are total pressure and velocity, respectively. This figure also shows the experimental results from Reference [5] and results obtained from computations using the method of streamline curvature^[6].

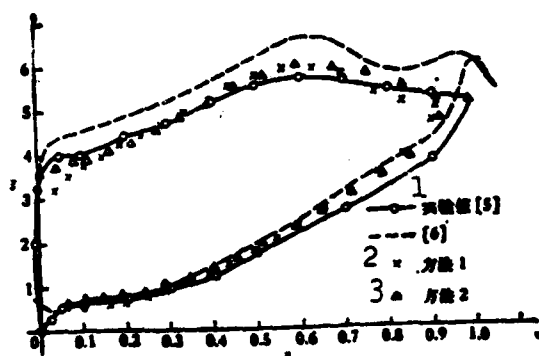


Figure 4.

Key: 1) experimental values; 2) Method 1; 3) Method 2.

As compared with the experimental results, the results obtained by Method 2 for the front edge of the blade back are improved over those obtained by Method 1. It is obvious that agreement with the experimental data is better for the results obtained using either

method than those obtained in Reference [6]. The upstream and downstream Mach numbers of the cascade and the downstream flow angle β_2 as calculated using these three methods are tabulated in Table 1. The values obtained using Method 2 has the smallest deviation from the experimental data. In addition, the calculations show that, even for this kind of subsonic cascade, there is still a substantial difference between the total pressure on the surface and the total pressure upstream. Figure 5 gives a comparison between the total pressure on the surface as calculated from Method 1 and that calculated from Method 2. The deviation for the latter is very small.

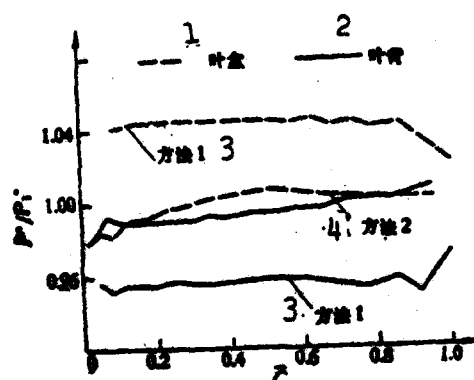


Figure 5.

Key: 1) blade back; 2) blade basin; 3) Method 1;
4) Method 2.

2. NACA Transonic Turbine Blade Cascade with 95° Deflection Angle

The turbine blade cascade with 95° deflection angle as given in [5] contains a region in the blade back where the flow speed

exceeds the speed of sound. We used Method 1 and Method 2 to calculate a case where the blade stagger angle is 28.1° . The pressure coefficient on the surface is as shown in Figure 6. In comparison with experimental data, the pressure coefficients given by Method 1 tend to be on the high side for both the blade back and the blade basin. Better results were obtained with Method 2. The values for M_1 , M_2 and β_2 computed by either method are shown in Table 2. Here again, the results obtained by Method 2 agree closely with experimental data.

Table 1.

	1 实验值[5]	2 方法 1	3 方法 2	[6]
M_1	0.319	0.326	0.317	0.319
M_2	0.801	0.796	0.793	0.846
β_2	-58.2	-57.2	-57.7	-58.4

Key: 1) Experimental Values [5]; 2) Method 1; 3) Method 2.

Table 2.

	1 实验值[5]	2 方法 1	3 方法 2
M_1	0.409	0.40	0.409
M_2	0.943	0.93	0.947
β_2	-55	-56.6	-55.46

Key: 1) Experimental Values [5]; 2) Method 1; 3) Method 2.

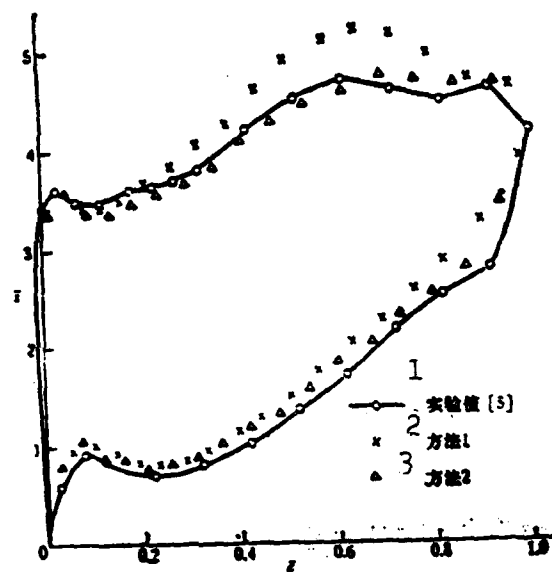


Figure 6.

Key: 1) Experimental values [5]; 2) Method 1; 3) Method 2.

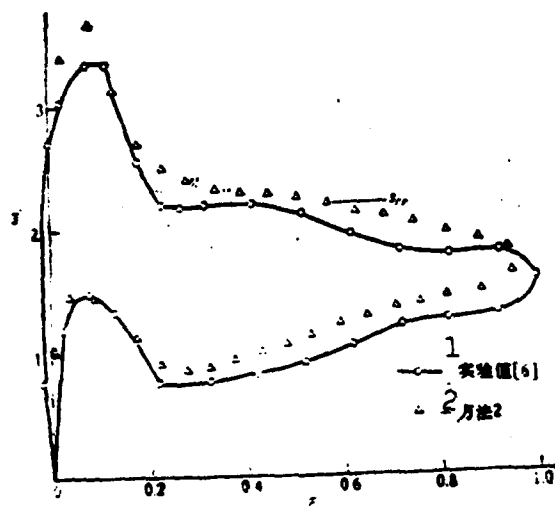


Figure 7.

Key: 1) Experimental values [6]; 2) Method 2.

3. NACA Transonic Turbine Blade Cascade with 95° Deflection Angle in the Presence of Shock Waves

The experimental results for this kind of blade cascade at high speeds as given in [5], show that shock waves appear in a region at 20% chord length, causing a sharp drop in the pressure coefficient in that region. The coefficient of pressure on the blade surface as calculated by Method 2 is shown in Figure 7, where \bar{s}_{cr} denotes the critical pressure coefficient. The artificial viscosity used in the calculation is in the form given by Equation [22]. We see that the position calculated for the shock wave agrees basically with that obtained experimentally. The profile of the distribution of the pressure coefficient is in fair agreement with the experimental data, but the values tend to be on the high side.

VI. METHODS FOR INCREASING THE RATE OF CONVERGENCE

The above computational examples show that satisfactory results are obtained by applying Method 2 to the computation of the transonic cascade flow field. However, it usually takes a great many time steps before stability is reached if one adopts this method. It is necessary, therefore, to increase the rate of convergence so as to enhance computational efficiency.

In a certain sense, the time-dependent scheme is similar to the relaxed methods used in solving boundary value problems involving elliptical partial differential equations. In other words, no matter how the initial field is specified, as long as it is compatible with the given physical problem, a unique stable and constant solution can be found in due course. Hence, when it is only necessary to solve for the stable, constant flow, the time step size used in the computation does not have to be the

same for every point in the flow field. One does not need to take the smallest allowable time step size of the entire field as the common time step size. Instead, one can use the local allowable time step size to do the computation at each point in the flow field. (In the time-splitting scheme, use the smaller of $\Delta t_{s_{1,j}}$ and $\Delta t_{y_{1,j}}$ at each point.) Thus, as time advances, the instantaneous solution of the flow field will be distorted. Yet, as a steady state is approached, the asymptotic solution will be correct. The use of the maximum allowable time step size at every point will greatly reduce the number of time steps required before reaching the steady state. In our computations, we have used this method to great advantage. Moreover, to further increase the rate of convergence, we have used the method of gradually reducing the size of the mesh unit. The approach has also reduced time required for computation.

Table 3.

	① 使用全场统一的时间步长, 网格不加密	② 使用当地时间步长, 网格不加密	③ 使用当地时间步长, 网格加密 40×7→40×14
④ 达到收敛的步数	1260	840	580+360
⑤ 计算时间的相对值	100%	67%	52%

Key: 1) Same step size for all points, mesh unrefined; 2) local step size, mesh unrefined; 3) local step size, refined mesh 40x7→40x14; 4) steps required for convergence; 5) relative value of computation time.

Table 3 shows the effect of using the above methods to increase rate of convergence. The example used in the computation is that of the NACA transonic turbine blade cascade with 95° deflection angle and with blade stagger angle of 28.1°. Mesh was taken to be

40x14. We see that a 35% reduction in the time required for convergence is effected by using the local allowable time steps /129 instead of a common time step for all points in the field. Refining the mesh once (from 40x7 to 40x14) and at the same time using the local allowable time steps in the computations, has cut down the time required for obtaining the steady state solution to almost half of its original value. By using Method 1, taking mesh to be 41x7, one can meet the condition of $|(V_i^{n+1} - V_i^n)/V_i^n| \leq 10^{-4}$ after 800 steps, in general. Computation time is 15 minutes on the TQ-6 computer. The same degree of convergence can be achieved by using Method 2 and refining the mesh once (from 40x7 to 40x14), after about 20 minutes of computation.

REFERENCES

- [1] Denton, J. D.: A Time Marching Method for Two and Three-Dimensional Blade to Blade Flows, *AEC RM*, 3775, (1975).
- [2] MacCormack, R. W. and Paullay, A. J.: Computational Efficiency Achieved by Time Splitting of Finite Difference Operators, *AIAA Paper*, 72-154, (1972).
- [3] Richtmyer, R. D. and Morton, K. W.: Difference Methods for Initial-Value Problems, 2nd Edition, Interscience Publishers, New York, (1967).
- [4] Hung, C. M. and MacCormack, R. W.: Numerical Solutions of Supersonic and Hypersonic Laminar Compression Corner Flows, *AIAA J.*, 14, 4, (April 1976).
- [5] Dunavant, J. C. and Frwin, J. R.: Investigation of a Related Series of Turbine-Blade Profiles in Cascade, *NACA TN*, 3802, (1956).
- [6] Wilkinson, D. H.: Calculation of Blade-to-Blade Flow in a Turbomachine by Streamline Curvature, *AEC RM*, 3704, (1972).

A SURGE TEST OF A TWIN-SHAFT
TURBOJET ENGINE ON GROUND TEST BED*

Chiang Feng
(Shengyang Aeroengine Company)

ABSTRACT

Instrument technique for determining the surge point of a twin-shaft turbojet engine on a ground test bed is presented in this paper. The effectiveness of two surge-inducing methods used in the test is also described in the paper. A practical fuel flow step unit is introduced and the surge point measurement and the trace analysis of the engine operating point are discussed.

Typical oscillograms are given which were taken when the engine was surging or not surging during the fuel flow stepping. When the engine was brought into surging, the engine operating point trace diagram was determined by a calculation method based on the flow continuity through nozzle guide vanes of the turbine. This diagram is the final result of the surge point determination technique.

I. INTRODUCTION

In order to determine the characteristics of inlet and engine matching for more recent models of propulsion systems, one must obtain the surge margin of the engine in cases with or without distortions. The fundamental experimental techniques that need

/130

* This paper was read during the Third National Meeting of the Engineering Thermophysics Conference held in Kueilin in April, 1980.

to be studied first include surge inducement, determination of the surge point and calculation of the parameters of the surge point. Since we have had no previous experience in inducing surge in a twin-shaft turbojet engine that is capable of automatically preventing surge, we feel that an experimental study needs to be carried out.

II. TESTS ON INDUCING SURGE BY VARYING AREA OF NOZZLE

Any means by which the flow out of the compressor exit can be regulated may be used for inducing surge. The common methods used to induce surge in engines on a ground test bed are of three types: geometric, aerodynamic or thermodynamic regulation of the flow. Some examples are: varying the area of the nozzle and that of the nozzle guide vane passage, blowing air at the back of the compressor or squirting water into the combustion chamber, and using a fuel flow step unit. In our tests, we have chosen to induce surge by varying the area of the nozzle, and by using a fuel flow step unit.

From the principle of engine operation, we know that, by rapidly reducing the area of the nozzle, we can cause the temperature in front of the turbine to rise, and can thus possibly induce surge in the high-pressure compressor. Variations in the nozzle area are necessarily limited by the structure. We therefore turned to the technique of an "aerodynamic small nozzle", in which the actual nozzle size stays the same during reheating, while the effective area of the nozzle is reduced rapidly by suddenly increasing the reheat fuel supply, resulting in an increase in the counter pressure behind the turbine. The tests were performed at higher than 85% of rotational speed during small reheating. The rate of reheat fuel supply had been increased to several times its original value beforehand, and when the "nozzle" suddenly decreased

in area, the rotational speed of the high-pressure compressor rapidly rose, and the exhaust reached a temperature as high as 950°C . However, after several trials, we were unable to induce surge, while the temperature had increased to a value well above the allowable limit.

There have been some arguments regarding the possibility of inducing surge in the low-pressure compressor. To settle this question, we constructed a large nozzle with an area equivalent to 193% of that of the "largest" nozzle under normal conditions. Many tests were performed, in which the nozzle area was reduced and increased alternately for many times. The reheat was suddenly terminated after it was turned on at reduced rotational speed, and the speed was sharply reduced. All this was done to see if surge could be induced when the operating point of the low-pressure compressor underwent an abrupt change when the surge margin was approached. However, the engine never surged in the range of 80-100% of rotational speed. Measurement of the low-pressure compressor operating line has shown that the shift on the operating line, produced by doubling the area of the nozzle, was very small; the surface pressure behind the turbine had already decreased to zero. When the low-pressure rotational speed was 100%, the high-pressure rotational speed was 88%; the exhaust temperature was as low as 430°C . In summary, we were not able to induce surge by introducing a maximum possible mismatch between the high-pressure and low-pressure rotational speeds to vary the flow in the low-pressure compressor. The above two tests of varying the nozzle size have indicated that the twin-shaft engine has a high capability of preventing surge. Changing the area of the nozzle within the limits of allowable testing temperatures and structural conditions did not result in surge of the engine during equilibrium or transient operation. The surge allowance for the high-pressure and low-pressure compressors on a ground test bed was much larger than that required when the engine underwent abrupt changes in conditions. There was

/131

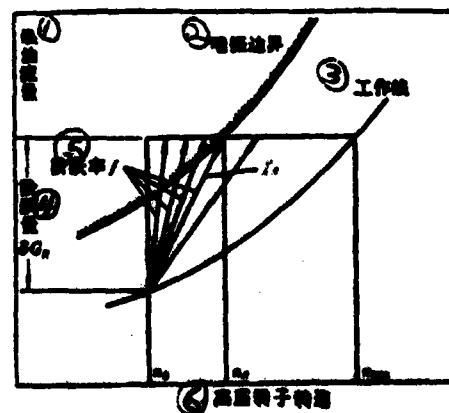
only one thing that was unusual, viz. when the rotational speed was increased at the same time reheat was turned on for the large nozzle at low rotational speed, a strange noise emanated from the engine when the low-pressure rotational speed was in the 88-82% range. However, no stall signal was found on the oscillogram for the static pressure behind the two compressors. This noise was analyzed and believed to have arisen from the vibrations of the rotating blades in the first stage.

III. SURGE INDUCEMENT USING FUEL FLOW STEP UNIT

Fuel flow stepping is the process of suddenly squirting into the combustion chamber an extra jet of fuel for over 0.4 seconds, at a stable rotational speed. It is the main technique for inducing surge in the engine by the sudden thermodynamic flow regulation in the nozzle guide vanes of the turbine. Figure 1 shows the principle of inducing surge in the high-pressure compressor using fuel flow stepping. When the fuel flow step amount δG_R is at a certain value, any fuel flow stepping rate $f = dG_R/dn$ that is higher than f_A will cause the engine to surge at a certain rotational speed in the range $(n_A - n_B)$.

Figure 1. Principle of surge inducement by fuel flow stepping.

Key: 1) fuel flow amount; 2) surge margin; 3) operating line; 4) fuel flow step amount; 5) fuel flow stepping rate; 6) rotational speed of the high-pressure rotor.



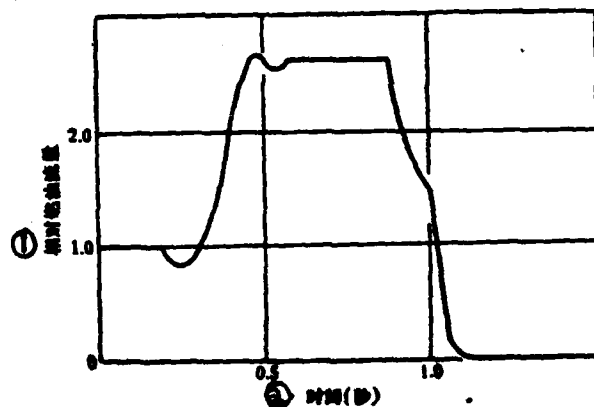
The higher the fuel flow stepping rate, the lower the rotational speed at which the engine will be brought into surging. At the same fuel flow stepping rate, the larger the fuel flow step amount, the higher the maximum rotational speed n_A at which the engine can be brought into surging. Upon fuel flow stepping, the high-pressure compressor stage that first goes into surging produces forward impact waves in a manner similar to a flow regulating valve that is suddenly shut off. This brings the upstream stages into surging, one after another. Therefore, the low-pressure compressor always goes into surging a short moment after the high-pressure compressor starts to surge. Based on this principle, we have, after repeated modifications, successfully constructed a fuel step unit that is suitable for the twin-shaft engine.

The system in question was built by modifying and putting together two ground refuelling pumps and the main fuel regulator of an engine. It also has an electric control box, that automatically controls the fuel flow stepping time and the beginning and termination of engine surging. Before fuel flow stepping, the two pumps were allowed to operate at full speed for a brief moment, and the pressure was adjusted to over 90kg/cm^2 . When the switch to the fuel step unit was turned on, the system injected all the fuel from the pumps into the main fuel line of the engine. This enabled the engine to surge at below 75% rotational speed. By modifying the main pump regulator, we were able to increase the fuel flow step amount to over two and a half times its original value, and the rotational speed at which the engine can be reliably brought into surging reached 97%. These were the measures taken: The driving axle of the centrifugal pendulum of the rotational speed regulator was removed to eliminate the fuel reducing action in the process of fuel slow stepping. The high-pressure fuel was fed from the distributor to the right chamber on the slanted-disk valve via branch lines I and II (without throttle control). All the extra cavities and openings along the passage of the high-pressure fuel were blocked,

the control for limiting pressure increase was shut off, and the fuel in the left chamber of the valve was let out into the atmosphere so as to effectively increase the acceleration of the slanted disk toward the left. 0.15 to 0.2 seconds after the fuel flow step unit was turned on (when we also had to change to the highest shift). The fuel flow was stepped up to its maximum value, during which time surge was induced. The fuel flow stepping was kept on with a timed current control for 0.4-0.5 seconds, after which the fuel flow was automatically cut off, and surging was stopped. Figure 2 shows the variation with time of the fuel amount during fuel flow stepping.

Figure 2. Fuel amount during fuel flow stepping vs. time curve.

Key: 1) relative fuel flow amount; 2) time(second).



IV. MEASUREMENT SET-UP

Figure 3 is a schematic diagram of the testing system. The testing probes for the equilibrium and transient operations are arranged in such a way that the transient system can be corrected against the equilibrium system. The Pitot tube and the probe for measuring the transient total and static pressure difference are installed in the measurement section of the inlet. The sensors for total pressure, static pressure, and total temperature are placed at the exits of the low-pressure and high-pressure compressors

/132

and behind the turbine. The transient pressure is measured by means of a high-frequency-response solid pressure pick-up. Measurement accuracy is increased by the use of a system that contains no resonators, and by regional amplification. The transient temperature is measured with a low-inertia thermocouple. When this is compared to the pressure signal, there is a delay of 0.1-0.2 seconds. The amount of fuel flow is calculated from values obtained for the transient pressure in the main and auxiliary fuel lines. The transient fuel flow amount is corrected against the equilibrium fuel flow amount measured on a ground test bed. All the parameters of the transient state are recorded with two oscilloscopes and one magnetic tape recorder. The equilibrium pressure is recorded with the SYD-1 and XJ-100 testing equipment. The rest of the parameters are measured using the test equipment that comes with the test bed.

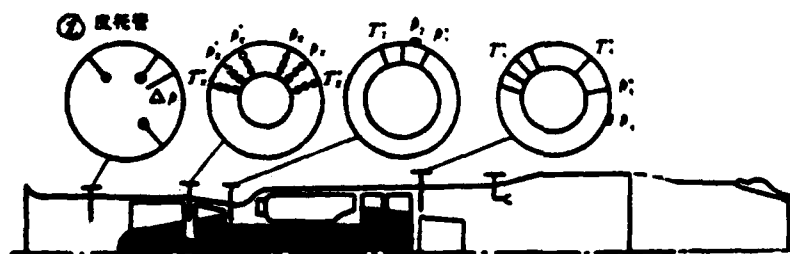


Figure 3. Diagram of the testing system.

Key: 1) Pitot tube.

Note: Δp : probe for measuring transient total and static pressure difference;

p_x^*, p_x, T_x^* : total pressure, static pressure and total temperature at exit of the low-pressure compressor;

p_2^*, p_2, T_2^* : total pressure, static pressure and total temperature at exit of high-pressure compressor;

p_4^*, p_4, T_4^* : total pressure, static pressure and total temperature at exhaust.

V. SURGE

When the fuel flow step unit is turned on at a chosen equilibrium rotating speed (called the starting condition for surging), one immediately sees a flare of orange-red flame at the tailpipe of the engine. At the same time, single or multiple booms are heard. The vibrational energy of the surge is enormous, especially in the range of 85-90% of rotational speed. One can feel the vibrations in the control room and even in other more remote parts of the plant. These earthquake-like vibrations have caused nearby test parts to drop to the ground, and have even upset a stand for hanging weights that weighs several tens of kilograms. It is obvious that the surge should not be allowed to last for a long time, and its danger and destructive ability should be taken into account.

/131

Figure 4. Variations in parameters before, during and after surge.

Key: 1) time(sec).

Note: p_{TZ} : pressure in the main fuel line;
 p_{TF} : pressure in the auxiliary fuel line;
 n_1 : rotational speed of the low-pressure rotor;
 n_2 : rotational speed of the high-pressure rotor;
 C : surge point;
 p_x, p_2^* : same as Figure 3.

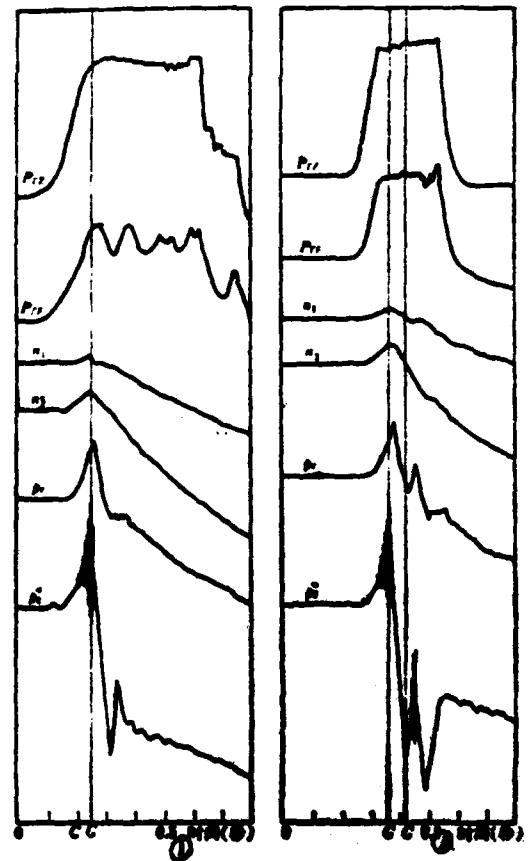


Figure 4 shows two diagrams that are typical of the recorded curves for the 42 surges in our tests. These diagrams show the variations in parameters before, during, and after the engine surge as well as the surge characteristics. The essential points are summarized as follows:

1. The entire process of surge inducement by fuel flow stepping takes place in a very short time, about 0.5-0.7 seconds only. Thus any damage to the engine blades or other structural elements will be minimal.

2. Because of the high rotational inertia of the high-pressure and low-pressure rotors, there is only a small sudden increase in rotational speed that does not exceed 3-4%. This sudden rise in rotational speed is mainly related to the rate of fuel flow stepping.

3. It takes about 0.03-0.10 seconds for the exit pressure of the high-pressure and low-pressure compressors to rise from the equilibrium operating point to the surge point. This corresponds to an acceleration much higher than that of a normal engine. Whether the sharp increase in the angle of attack will cause difficulty in the determination of the surge point has been one of our concerns. This possibility has been dismissed after some analysis. Any appreciable stalling or delay usually occurs when the rotating blades sweep over the edge of the region of distortion, causing an abrupt change in the angle of attack. This takes place in the range of time during which the rotor has made a fraction of a revolution (0.5×10^{-3} - 0.6×10^{-3} sec.).

4. Before the high-pressure compressor starts to surge, there always appears a rotating stall wave. During the peaking of the wave, the average value of the compressor exit pressure keeps rising for a period time and then suddenly drops, whereupon

the engine starts surging. Some stall waves are divided into two parts, with a very short rest period in between. The first part is only accompanied by stalling, while surge occurs during the second part. Hence, stalling presignifies high-pressure compressor surge. This conclusion from experimental tests has a great significance for this type of engine. It provides the condition based on which a system containing a stall alarm and surge while still in the stage of rotational stall, by controlling pulsed fuel supply, and thus avoiding a breakdown during flight. /134

5. The low-pressure compressor surge results from the impact wave generated by the high-pressure compressor surge. The surge point of the former is delayed by about 10 milliseconds with respect to that of the latter. No stalling has occurred before, during, or after the low-pressure compressor surge.

6. The number of peaks in the surge wave varies with experimental conditions. In the 42 surges, the majority of surges contain only one peak accompanied by a single boom. There is a considerable number of double-peak surges (accompanied by double booms). Only one multi-peak surge has been observed, and that was caused by a prolonged fuel flow stepping time. The surge peaks are separated in time by a period of about 0.1 seconds. In other words, the frequency of vibration of the axial flow arising from the surge (which takes the form of forward impact waves and backward expansion waves) is 10 hertz.

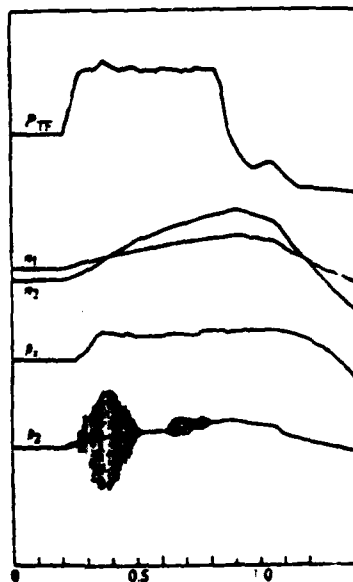
VI. STALLING

When the fuel flow stepping rate is small or when the fuel step amount is insufficient as required by the rotational speed, the engine rapidly accelerates but does not go into surge, as

shown in Figure 5. From this, the engine operating point trace diagram can be calculated for the condition of maximum acceleration, and used in the determination of the surge margin. The oscillograms show that during the rapid acceleration, the exit pressure of the high-pressure compressor has twice shown progressive type stalling. From this and the stalling that occurs before a massive surge, we conclude that there exists a stall margin beneath the surge margin of this high-pressure compressor that can be determined by slowly bringing the engine into surge. The stalls that occur at two places in the curve are not accompanied by jets of fire or booms, nor is there any appreciable amount of low-frequency vibration, and all parameters of the oscillogram keep rising steadily during the stalls. This proves that surge and stall are two different physical phenomena and should not be confused.

Figure 5. Oscillogram for fuel flow stepping during which surge was not induced.

Key: 1) time(sec).



VII. DETERMINATION OF ENGINE OPERATING POINT TRACE DIAGRAM

Fuel flow stepping is a transient process during which the parameters undergo sharp changes. Whether or not the engine is brought into surge, the problem of engine operating point determination is more complicated than without fuel flow stepping. Although methods for solving sets of differential equations based on volume dynamics seem attractive, they are nevertheless too tedious when applied to the experimental data. The pressure ratio surge allowance determined from the experimentally measured pressure increase ratio vs. rotational speed relation can be conveniently used in ground test calculations. However, it will not be as easy to obtain the relation between the amount of air flow and the pressure increase ratio (or rotational speed) because of the low accuracy for the direct measurement of the instantaneous air flow. Therefore, a method based on the flow continuity through the nozzle guide vanes of the turbine is recommended in [2]. Although the computer program for this method is long and involved, the method has been chosen because it is the "most accurate" method for determining operating line deviations during sudden changes in the engine. We have thus written an ALGOL-60 program and used it to make some initial calculations for the surge line and the parameters for the surge point.

Based on our present test conditions, the experimentally measured parameters that can be used in the calculations for the transient state are fuel pressure, pressure at the inlet and exit of the compressor, and rotational speed. As the time constant of the thermocouple used for temperature measurement is too large, the temperature has been determined from calculations rather than actual measurements. The effects of engine volume dynamics and rotational inertia have been neglected. The efficiency characteristics are assumed to be the same for the entire engine as well as for each individual compressor. During the instantaneous changes,

/13

the law of flow continuity is assumed to hold true for each section. On the basis of the above conditions, the computational steps are given as follows: At a certain instant during fuel flow stepping, the inlet flow amount and the exit temperature of the low-pressure compressor are given the assumed initial values G_0 and T_X^* . Then, the actually measured exit static pressure p_x is used to obtain the total pressure and the stagnation pressure increase ratio $\pi_{k.dy}^*$. The efficiency and the exit are determined from known low-pressure compressor characteristics, and the temperature TA_X^* is calculated. The inlet flow conversion is obtained for the high-pressure compressor, and the pressure increase ratio $\pi_{k.gy}^*$ is calculated from the measured exit total pressure p_2^* . The exit temperature T_2^* is obtained from the efficiency given in the high-pressure compressor characteristic curve. The temperature T_3^* in front of the turbine is then calculated from the instantaneous fuel flow amount determined from the actually measured fuel pressure. The amount of air flow G_d that is allowed to pass is calculated by solving the equation of flow continuity of the nozzle guide vanes of the choke. If G_d equals the initially assumed value G_0 for the low-pressure compressor inlet flow, and at the same time the calculated temperature value TA_X^* is equal to the assumed value T_X^* , then the computation for that point is completed. Otherwise, the iterative substitution is continued until both of the above conditions are satisfied. If we divide the duration of the fuel flow stepping into time steps of 0.01-0.02 second each, and repeat the above calculations for each computational point thus formed, the trace diagram can be readily obtained for the operational point. If this is the surge line, then the values of the last point are the surge point parameters. Computed examples are given in Figures 6 and 7. The surge allowances for the pressure increase ratio at equal flow for the high-pressure and low-pressure compressors are respectively 8.9% and 10.3%. This is fundamentally in agreement with experimental data. The surge margin obtained by computing for several surge

points has a reasonable tendency, and agrees on the whole with experimental results. These curves are given in the test reports on inlet flow distortions of said engine, and will not be duplicated here.

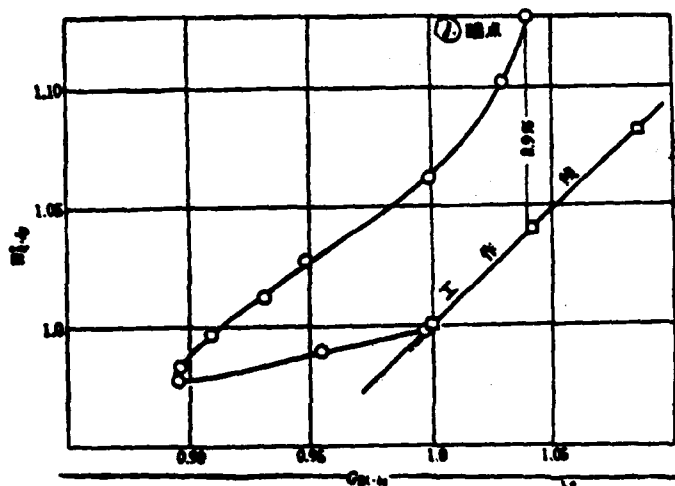


Figure 6. Surge line for the low-pressure compressor.

Key: 1) surge point.

Note: $\pi_{k,dy}^*$ is the relative stagnation pressure increase ratio of the low-pressure compressor;

$G_{B1.ks}$ is the inlet relative conversion air flow of the low-pressure compressor.

The purpose of this paper is to obtain via an experimental study, technical methods for surge-inducement, surge measurement and surge point determination that can be effectively applied to a twin-shaft turbojet engine on a ground test bed. The primary purpose has been achieved herewith. Any imperfections that exist should be taken up in future studies.

The following comrades also participated in the experimental work: Liu Chi-ch'en, Chou Yü-wen, T'en Shou-chen, Chiang Hsün-yi and Shih Yeh-lin.

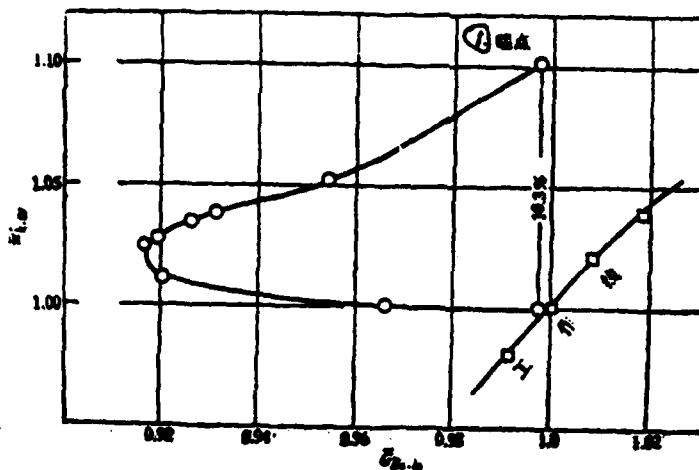


Figure 7. Surge line for the high-pressure compressor.

Key: 1) surge point.

Note: $\bar{\pi}_{k.gy}$ is the relative stagnation pressure increase ratio of the high-pressure compressor;

$\bar{G}_{Bx.kg}$ is the inlet relative conversion air flow of the high-pressure compressor.

REFERENCES

- [1] H. C. Melick, Jr. and W. E. Simpkins: A unified theory of inlet/engine compatibility, AIAA, 79-1115.
- [2] K. Kovach, P. E. Griffiths: Engine compression system surge line evaluation techniques, General Electric CO. paper No. 76-015.

EFFECT OF BLADE STAGGER ANGLE ON PERFORMANCE OF A TRANSONIC COMPRESSOR WITH LOW HUB-TIP RATIO*

Chao Shih-ch'un
(Shenyang Aeroengine Research Institute)

ABSTRACT

The effect of blade stagger on the performance of a transonic compressor with low hub-tip ratio is presented in the paper. Because the original single stage compressor failed to achieve the design target, tests were conducted on the compressor with blades twisted and with the stagger angle reduced. The results of these tests indicate that at the design speed and mass flow, the pressure ratio is 1.339, the efficiency is 0.864, which is 2.2% better than the design value and 5% better than that of the original single stage. At the same time, the discharge total pressure and temperature profiles are improved substantially. The unevenness of the total pressure profile decreases from 18% to 7% and that of the total temperature from 53% to 18%. The operating point of the compressor has been moved from the left branch to the right branch of the characteristic line and is located in high efficiency region.

I. INTRODUCTION

The single stage in question in a transonic compressor with low hub-tip ratio. Experimental results show that: stage torque efficiency $\eta_m^* = 0.82$ which is lower than the design value by 2.8%. The unevenness in the pressure field and temperature field of the stage exit is 18% and 53%, respectively, which is far from meeting

* This paper was read during the Third National Meeting of the Engineering Thermophysics Conference held in Kueilin during April, 1980.

the design requirement. The experimental operating point lies in the left branch of the characteristic line. Because of the presence of vibrations in the test sample, we did not carry out an experiment on surge margin.

Because this single stage did not meet design requirements, the performance of the entire engine was affected. In order to improve the performance of this first stage, in addition to the tests done on this stage, we also carried out tests in which the rotating blades were twisted ($0-3.5^\circ$) along the line from the average radius to the blade tip, or the stagger angle was reduced by 3° (with the blades twisted). We shall refer to these two types of tests as twisted-blade tests and reduced-stagger angle tests, respectively. Experimental results show that, after the adjustments, the single stage was able to meet design requirement, there was marked improvement in the pressure field and temperature field of the stage exit. The operating point was shifted to the right branch of the characteristic line. The above results have provided a basis for the design of the first stage.

II. AERODYNAMIC DESIGN

Following is a brief account of the design of the single stage. Parameters of the design point:

Relative air mass flow $\dot{W}=1.0$

Pressure increase ratio $R=1.34$

Efficiency $\eta=0.845$

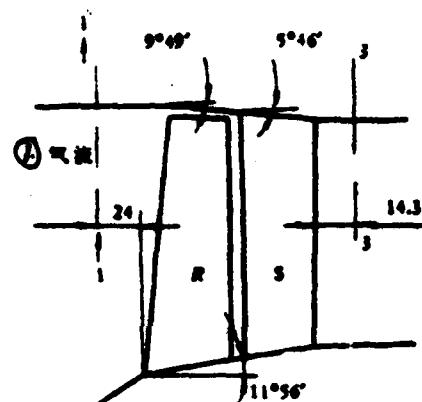
Relative Mach number of blade tip $M_t=1.204$

Hub-tip ratio $\bar{d}=0.385$

The shape of the passage approaches that of equal mid-radius.

Figure 1. Flow diagram for the stage passage.

Key: 1) air flow.



The stator and rotor both have a double-arc blade shape.

The gradients of enthalpy and entropy have not been taken into consideration in the design. Rather, we followed the design rule of maintaining isentropic conditions, constant work and constant annular quantity along the radial direction. The basic equations are the same as those given in Reference [2]. The radial equation of balance is:

$$r_s \frac{\partial v_s}{\partial r} = s \left(\frac{\partial H}{\partial r} - T \frac{\partial s}{\partial r} \right) - \frac{v_s}{r} \frac{\partial (v_s r)}{\partial r} + v_s \frac{\partial v_r}{\partial s}$$

The conditions of isentropy, constant work and constant annular quantity can be used to simplify the equation to:

$$\ln \frac{v_{s,i-1}}{v_{s,i}} = \left\{ \frac{(y'_{i-1} + y'_i) \left(y'_i - \frac{r_{i-1}}{r_i} y'_{i-1} \right)}{r_i \left[\left(\frac{r_{i-1}}{r_i} \right)^2 - 1 \right] \left[1 - \left(\frac{M_i + M_{i-1}}{2} \right)^2 \right]} + \frac{y''_i + y''_{i-1}}{2} \right\} (r_{i-1} - r_i)$$

In the above equation, $y' = dr/dz$ is the slope of the streamline, and $y'' = d^2r/dz^2$ is the second derivative of the streamline. The subscripts $i-1$ and i denote neighboring borders of the upper and lower flow pipes. $i=1, 2, \dots, 11$.

In the computation, assumed distributions of streamlines and Mach numbers are taken as initial values from which the distribution of v_m is found. The successive approximation is carried on until the chosen values agree with the computed values. Actually, in the design of this single stage, the Mach number used is that obtained from solving the simple radial equation of balance, and y' and y'' have been obtained by approximate methods of calculation.

The velocity distribution along the axial direction has been obtained by first solving the simple radial equation of balance, then modifying the results on the assumption that the streamlines are sine curves.

The shaping has been done by applying analytical methods to a cylindrical surface. First, the blade angle is found on the conical surface. Then the blade section angle is found by geometrical projection on the cylindrical surface.

$$\tan \alpha_{bl. \text{ angle}} = \tan \alpha_{bl. \text{ sec. angle}} \times \cos \epsilon$$

where ϵ is the angle between the velocity and the axial line in the meridian plane.

III. TESTS, RESULTS AND ANALYSIS

The compressor under test has a given power of 4000 hp and a given output rotational speed of 11175 rpm.

The test sample is a single stage transonic compressor.

The measurement set up is as shown in Figure 2.

Rotor inlet: p^* and p in the passage and the static pressure of the outer wall are measured.

Rotor exit: Only the static pressure of the inner and outer walls in the passage is measured.

Stage exit: The radial distributions of p^* , p , α , and T^* in the passage and the static pressure on the inner and the outer walls are measured. The accuracy of the meters is as follows.

rotational speed N	$\pm 0.2\%$	inlet temperature T_1^*	$\pm 0.7^\circ\text{C}$
mass flow W	$\pm 0.5\%$	exit temperature T_3^*	$\pm 1^\circ\text{C}$
torque M	$< \pm 1\%$	air flow angle	$\pm 1^\circ$
pressure p	$\pm 0.3-0.5\%$		

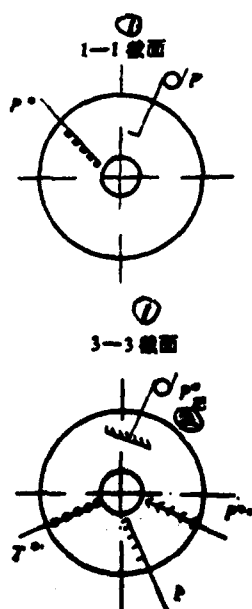


Figure 2. Placement of probes at inlet and exit.
Key: 1) cross-section; 2) harrow.

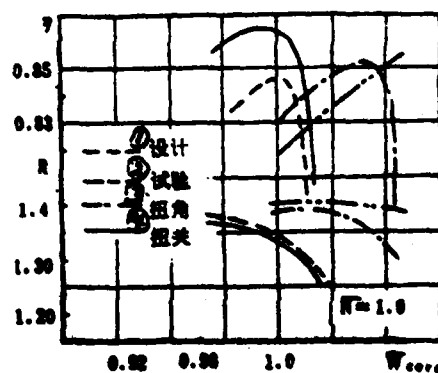


Figure 3. Characteristic lines of total performance of the single stage.

Key: 1) design; 2) experimental; 3) twisted-blade; 4) reduced-stagger angle.

Figure 3 gives the characteristic lines of the total performance of the single stage for different stagger angles. The curves $\bar{N}_{corr} = 1.0$ indicate that a design speed the twisted-blade arrangement has improved performance. Comparing the reduced-stagger arrangement with the original design, the mass flow at the choke point is reduced by 3.7%, and the operating point approaches the optimum point. The pressure ratio line is shifted toward the lower-left part of the diagram, and is in agreement with the design values. The efficiency line is shifted toward the upper-left part of the diagram, and is higher than the calculated envelope. The pressure ratio is 1.339 for $\bar{W}_{corr} = 1.0$, and meets the design value; $\eta_m^* = 0.864$ is higher than design by 2.2%, and the engine operates in a region of higher efficiency. /139

Figure 4 gives the radial distribution of the inlet parameters for $\bar{W}_{corr} = 1.0$ under different stagger angle arrangements. At design rotational speed and mass flow, tests on the original design, the twisted-blade arrangement and the reduced-stagger angle arrangement show that the flow field is uniform at the rotor inlet, and the radial distribution of \bar{M}_1 , λ_1^* and β_1 agrees with the design values, except that along the 5% streamline, λ_1 and \bar{M}_1 are a little higher than design. The amount of variation of the angle of attack along the radial direction is on the high side. In the reduced-stagger angle tests, this amounts to 3-6°.

Figure 5 shows the radial distribution of the flow field at the stage exit. The values of λ_3 for the original design and the twisted-blade arrangement differ appreciably from the design values, while λ_3 for the reduced-stagger angle arrangement is close to the design. The radial variation of the exit air flow angle agrees with the design in form, but is about 2° higher in magnitude.

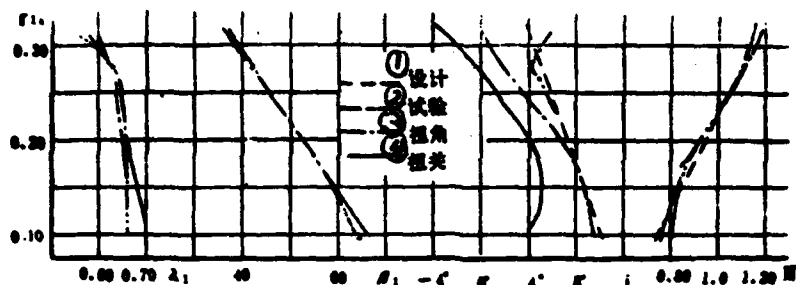


Figure 4. Radial distribution of inlet parameters for $\bar{W}_{corr}=1.0$ under different stagger angle arrangements.

Key: 1) design; 2) experimental; 3) twisted-blade; 4) reduced-stagger angle.

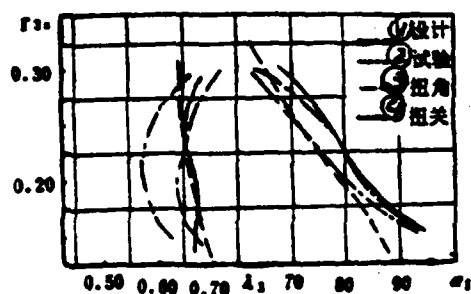


Figure 5. Distribution of flow field at stage exit.

Key: 1) design; 2) experimental; 3) twisted-blade; 4) reduced-stagger angle.

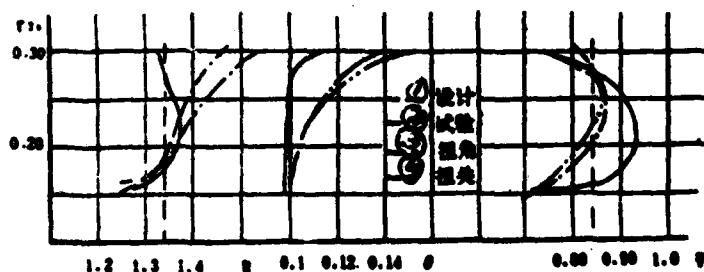


Figure 6. Radial distribution of blade performance parameters.

Key: 1) design; 2) experimental; 3) twisted-blade; 4) reduced-stagger angle.

Figure 6 shows the radial distribution of pressure ratio, temperature rise ratio and efficiency for the original single stage design, the twisted-blade arrangement and the reduced-stagger angle arrangement.

The diagrams show that the twisted-blade arrangement has an obvious effect on the performance of the compressor and the flow field at the exit. For a twist of 3° , in the 15-75% streamline region, the pressure ratio exceeds or is close to the design value of 1.34, and the efficiency exceeds the design value. However, the values at the blade root and the blade tip remain below designed values. /140

In summary, the original single stage has the following problems. $\eta_m^* = 0.82$ is below design. There is high unevenness in the stage exit pressure field and temperature field along the radial direction, which is 18% and 53%, respectively. The pressure ratio is low in the root region, where $R^* = 1.26$ on the 5% streamline. Mass flow at the choke point is on the high side; operating point is on the left branch of the characteristic line. The tests with the blades twisted and the stagger angle reduced by 3° show that the performance of the single stage is greatly improved. For $\bar{W}_{corr} = 1.0$, $R^* = 1.339$, $\eta_m^* = 0.864$; stage exit pressure field is reduced from 18% to 7%. The total temperature field is reduced from 53% to 18%. The pressure ratio on the 5% streamline is increased to 1.28. The characteristic line is improved. The operating point is shifted to the right branch of the characteristic line, and the engine operates in the vicinity of the high efficiency point.

We analyze the tests conducted on the compressor with the blades twisted and the stagger angle reduced by 3° as follows. After the stagger angle has been reduced by 3° , the performance of the single rotational speed and mass flow, the pressure ratio is 1.339, efficiency is 0.864 which is higher than design by 2.2%, and the efficiency is

higher by 5% than that of the original design. The twisted-blade reduced-stagger angle arrangement causes changes in the work done in the cascade channel, which in turn causes a redistribution of the velocity field. As a result, there is an obvious improvement in the stage exit flow field. The unevenness of the pressure field and the temperature field along the radial direction shows a marked decrease, with p^* dropping from 18% to 7% and T^* , from 53% to 18%.

The change in the blade stagger angle causes the cascade channel throat section to shift backward. The operating point of the blade row is changed accordingly. The characteristic line shifts toward the left. Compared with the original design, the mass flow at the choke point is decreased by 3.7%. Moreover, the location of shock waves at the root region is also changed, resulting in a reduction of loss. Hence, the efficiency at the root is increased and the operating point of the stage is located near the high efficiency point.

For the purpose of analysis, we give in Figure 7 the radial distribution of rotor blade performance. Figure 8 shows the relation between the parameters and \bar{W}_{corr} .

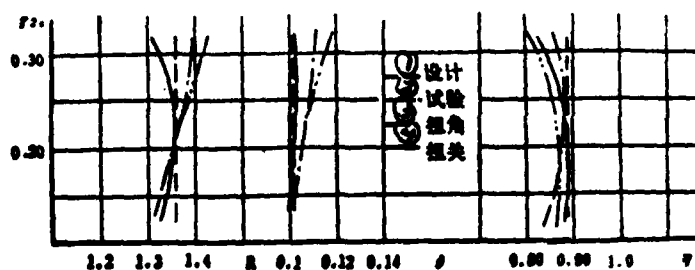


Figure 7(a). Distribution of primary performance of rotor blade.

Key: 1) design; 2) experimental; 3) twisted-blade;
4) reduced-stagger angle.

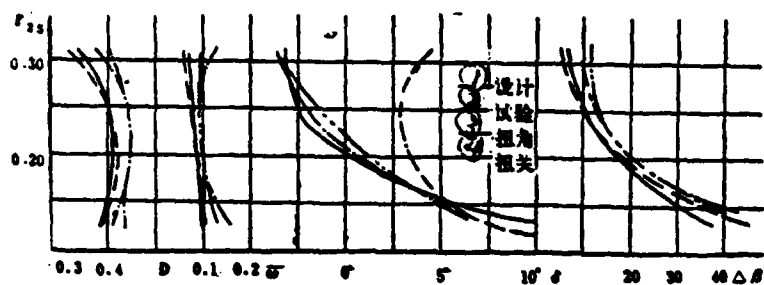


Figure 7(b). Variation along the radial direction of D , w , δ and $\Delta\beta$ of the rotor.

Key: 1) design; 2) experimental; 3) twisted-blade; 4) reduced-stagger angle.

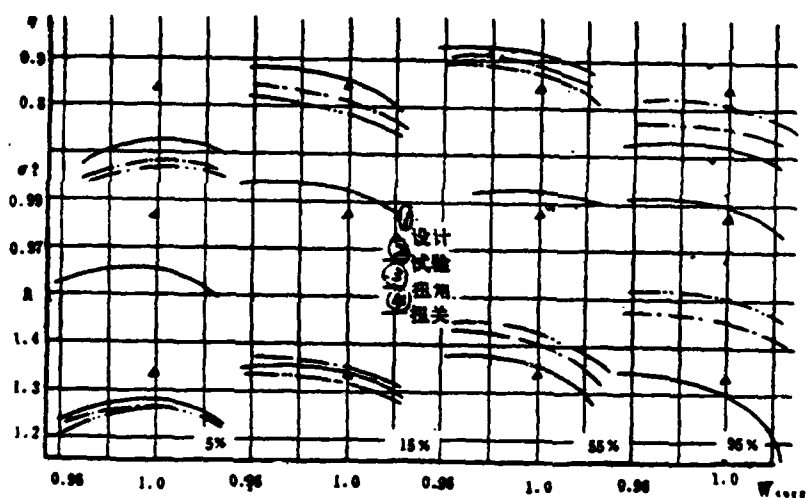


Figure 8. Relation between typical parameters on the streamline and \bar{W}_{corr} .

Key: 1) design; 2) experimental; 3) twisted-blade; 4) reduced-stagger angle.

On the 5% streamline in the blade root region:

Because of the small hub-tip ratio of the single stage ($\bar{d}=0.385$), the tangential velocity at the root region is low, the turn at the root is sharp, and the gas turns with difficulty. /141 The work done, the pressure ratio and efficiency are well below design values. Figures 4, 7 and 8 show that the 9.5° design angle of attack deviates from the optimal angle of attack for the hyperbolic blade shape, so that the root region operates in the separation region and the vortex region, and the diffusion factor and the loss coefficient are large. The computations show that the tolerance coefficient is small at the rotor root region. $A/A^*=0.96-0.97$, causing choke, resulting in increased loss. $M_v=0.87$ for the stator root region, causing the root region to operate^{x2} above the critical conditions. The loss is large, with $\sigma_s^*=0.95$. Hence on the 5% streamline, the pressure ratio reaches 1.26 and the efficiency is 0.67. /142 After the blades are twisted and the stagger angle is reduced by 3° , the additional work required is reduced for the rotor blade row. Because the angle of attack is reduced by about 5° , there is an appreciable decrease in the pressure ratio, and an appreciable improvement in loss. The diffusion factor and the loss coefficient approach design values. The efficiency of the rotor is 0.89. There is no improvement in the calculated value of $(A/A^*)_h$. Therefore, the increase in efficiency of the root region is chiefly attributable to the reduction in inlet angle of attack, and secondly to the backward shift of the throat section with the resulting change in location of the shock and a reduction in loss.

On the 15% streamline near the blade root region:

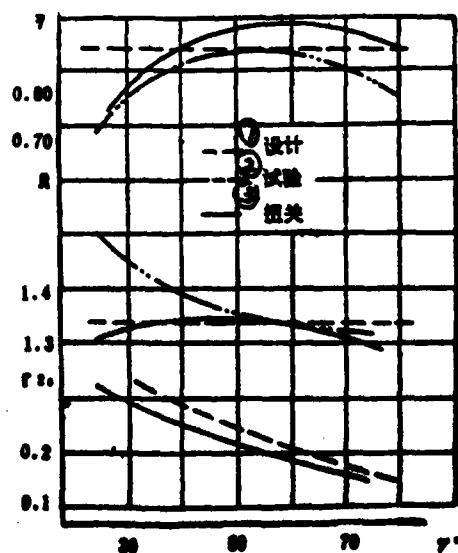
The angle of attack on this streamline is smaller than that of the original design by 3.6° . The deflection angle and lag angle are also reduced. The pressure ratio is below design value. This streamline is almost free of the effects of the root region, and is closer to the design conditions. Therefore, neither D nor $\bar{\omega}$ is large, approaching design values. $\eta_{ad}^*=0.90$.

On the 55% streamline in the average radius region:

Figure 9 shows that, when only the stagger angle is changed, while the other geometrical parameters are kept the same in the blade row, the pressure ratio does not drop much, but the efficiency is appreciably improved. This is mainly because the angle of attack of the rotor blade is closer to design and loss is reduced. Figure 7(b) indicates that when the stagger angle is reduced, $\Delta\beta$, δ_R are reduced, and the pressure ratio is lowered. On the other hand, the angle of attack selected in the original design was too high by 4° approximately, and D and $\bar{\omega}_R$ are large. If one can reduce the angle of attack, then the loss is reduced and D and $\bar{\omega}$ are appreciably decreased. Figure 8 shows that the stator blade has a small loss; $\sigma_s^* = 0.995$. Hence, both blade rows operate under better conditions, and the rotor efficiency reaches 0.92.

Figure 9. Relation between stagger angle and R^* and η_{ad}^* of rotor.

Key: 1) design; 2) experimental;
3) reduced-stagger angle.



On the 95% streamline in the blade tip region:

After the stagger angle is reduced by 3° , there is an appreciable reduction in $\Delta\beta$ and δ_R . The angle of attack of the tip section is reduced by about 6.5° . There is a relatively large decrease in R_t^* . At the same time, the angle of attack deviates from the optimum. Operating under the condition of negative angle of attack results in an increase in loss. In addition, there are shock and surface layer and second-degree flow losses that increase D and $\bar{\omega}$. $\eta_s^* = 0.98$ for the stator. Therefore the tip region has a low efficiency of 0.73.

The reasons for increased single stage efficiency after a 3° reduction in stagger angle can be summarized as follows. (1) The tests show that, after a 3° reduction in stagger angle, the angle of attack is close to optimum in the region between 15% and 75% streamline along the height of the blade. D is less than 0.40. On the 15-75% streamlines, α is less than 0.10 , which is close to design. The average efficiency of the rotor is 0.89. The root and tip regions operate under less favorable conditions and still have relatively low efficiency. (2) When the other geometric parameters of the cascade are kept the same and the stagger angle is $40-70^\circ$, there is not much decrease in the pressure ratio. However, because of reduced loss, there is an obvious increase in efficiency. Figures 6 and 7(a) show that the variation of R^* and θ^* along the height of the blade tends to be uniform and approximates the variations under the condition of constant work. This is close to the design condition. There is also an increase in η_{ad}^* .

IV. CONCLUSION

1. The test performed with the stagger angle reduced by 3° show an appreciable improvement in the performance of the single

/14

stage. At the design rotational speed, the pressure ratio is 1.339. The efficiency is 0.864, higher than design by 2.2%. There is substantial improvement in the stage exit pressure field and temperature field, the former dropping from 18% to 7% and the latter, from 53% to 18%. The characteristics are fine. The operating point has shifted from the left branch to the right branch, and is close to the high efficiency point.

2. Some problems that exist in the reduced-stagger angle tests are: The tip region of the rotor has a negative angle of attack; the root region of the rotor has a small tolerance coefficient, $A/A^* < 1.0$; the root region of the stator has a high $M_{v_{z_2}}$, and operates above the critical condition.

3. We suggest the following measures for improvement: (a) increase the hub-tip ratio or increase the tangential velocity in the root region. (b) Make appropriate adjustments in the choice of blade section parameters. For the double-arc blade section with $\bar{M}_t = 1.20$, we recommend a $0-2^\circ$ angle of attack for the blade tip, $3-4^\circ$ for the middle section and $4-5^\circ$ for the root. (c) In order to reduce or eliminate choke in the root region so as to increase the efficiency, a certain density has to be ensured. We recommend taking $A/A^* = 1.04-1.05^{[4]}$. (d) Use the multi-arc blade section for the root region of the stator, or use the double-arc blade section with appropriate adjustments in the parameters.

NOTATIONS

A/A^* ratio of actual area to critical area
 C chord length (meter)
 D diffusion factor
 \bar{d} hub-tip ratio
 β relative air flow angle (degree)

H enthalpy
 $\Delta\beta$ deflection angle (degree)
 i angle of attack (degree)
 γ blade stagger angle (degree)
 M Mach number
 δ° lag angle (degree)
 N rotational speed (rotation/minute)
 η_m^* stage torque efficiency
 $p^*(p)$ total (static) pressure (kg/cm^2)
 η_{ad}^* stage insulation (temperature rise) efficiency
 R pressure ratio
 θ^* total temperature increase ratio
 r radius (meter)
 σ density
 s entropy
 σ^* total pressure recovery coefficient
 T temperature
 \bar{w} coefficient of total loss
 t_m maximum relative thickness
 λ velocity coefficient
 v absolute velocity (m/sec)
 W mass flow (kg/sec)
 z axial distance (meter)
 α absolute air flow angle (degree)

SUBSCRIPTS

ab	absolute	ad	adiabatic
av	average	corr	correlated
h	blade root	m	meridian
s	stator	ST	stage
t	blade tip	R	rotor
		-	relative

r, z, θ denote radial, axial and tangential, respectively
1,2,3 denote rotor inlet, rotor exit and stator exit, respectively.

SUPERSCRIPTS

- * stagnation or total
- *^a in the direction of the total pressure

REFERENCES

- [1] Wu Chung Hsu: A General theory of three-dimensional flow in subsonic and supersonic turbomachines of axial, radial, and mixed flow types, ASME paper 50-A-79; trans. ASME, Nov. 1952 or NACA TN 2604, 1953.
- [2] James E. Hatch and Daniel T. Bernatowicz: Aerodynamic design and over-all performance of first spool of a 24-inch two-spool transonic compressor, NACA RM E56L07a, March 4, 1957.
- [3] D. R. Seyler and L. N. Smith, Jr.: Single stage experimental evaluation of high Mach number compressor rotor blading. Part I-design of rotor blading, NASA CR-54581, GE E06FPD821, April 1, 1967.
- [4] H. E. Messenger and E. E. Kennedy: Two-stage fan 1. Aerodynamic and mechanical design, NASA CR-120859, PWA-4148, 1972.
- [5] A. H. Epstein, J. L. Kerrebroek, and W. T. Thompkins, Jr.: Shock structure in transonic compressor rotors, AIAA, March/April, 1979.

THE STAGE MATCHING PROBLEM AND OPTIMIZATION ANALYSIS OF MULTI-STAGE TURBINES*

Ke Man-ch'u

(Institute of Engineering Thermophysics, Academia Sinica)

ABSTRACT

On the basis of the three-dimensional flow theory developed by professor Wu, the matching between turbine stages is discussed. The correlations of areas ratio, Mach number, vortex and angle of gas flow, as well as the correlations of expansion ratio, vortex and relative choke ratio are derived. We have obtained the change in performance of turbine stages affected by the position of the critical section. Moreover, we can control the performance of every stage of turbines and match the performance of every row of blades by arranging relative choke ratio effectively. From the calculation it is seen that when the position of critical section shifts to the following stage, the preceding stage performance becomes bad. When the stationary and rotating blades belong to the profile shape of the same type and the relative choke ratio of stationary blade row is equal to that of rotating blade row, the turbine stage efficiency is the highest.

On the basis of the theory of three-dimensional flow in blade-turbine systems, we derived the equation relating the design parameters and the flow parameters, and arrived at some useful conclusions from our computation of multi-stage turbine performance. The results of computations show that, by controlling the relative choke ratio of each section, one can effectively control the shape

*This paper was read during the Third National Meeting of the Engineering Thermophysics Conference held in Kueilin during April, 1980.

of the blade passage of the various stages and allow the various stages to operate at their highest capability. High efficiency can thus be obtained, the highest efficiency being obtained when the relative choke ratio approaches 1.

1. Equation Relating the Design Parameters and the Flow Parameters

$$\frac{dF_2}{dF_1} = [1 - f_1(M_1) \sqrt{\kappa g_c R T_1^2} \sin \beta_1 u_1 / H_1 g_c J + u_1^2 / 2 H_1 g_c J]^{\kappa_1} f_1(M_{w_1}) e^{-(s_1 - s_2)/R} / f_1(M_2)$$

in which

$$\begin{aligned} f(M) &= M / [1 + (\kappa - 1) M^2 / 2]^{\kappa_1} \\ f_1(M) &= M / \sqrt{1 + (\kappa - 1) M^2 / 2} \\ \kappa_1 &= (\kappa + 1) / 2(\kappa - 1) \\ w_1 &= [H_2 / (H_2 + f_1(M_{w_1}) \sin \tau_1 \sqrt{\kappa g_c R T_1^2} u_1 \\ &\quad \sqrt{1 - (2 f_1(M_2) \sqrt{\kappa g_c R T_1^2} \sin \beta_2 u_2 + u_2^2) / 2 g_c J H_2 / g_c J} \\ &\quad - f_1(M_2) \sqrt{\kappa g_c R T_1^2} \sin \beta_2 u_2 / g_c J + u_2^2 / g_c J)]^{\kappa_1 / (\kappa - 1)} e^{-(s_1 - s_2)/R} \end{aligned}$$

2. Critical Section and Choke

One of the most effective ways to increase the enthalpy drop in the single stage turbine is to employ transonic turbines. With the emergence of the transonic turbine, one must take into consideration the positioning of the critical section. When choosing the position of the critical section for a multi-stage turbine, one has to consider the combined effect of the performance of every

single stage, the efficiencies of the various stages, the matching of the various stages and their performance under varied operating conditions. If the critical section is placed in the first stage at the throat, then the merits of the first stage can be fully utilized. Good performance of the following stages can then be ensured by proper stage matching. If the critical section is placed in one of the following stages, then the performance of the preceding stages will be restricted. For example, in our computations for a multi-stage turbine, we found out that, if the blade stagger angle was reduced by 2° in the third stage turbine, the critical section was shifted to the third stage, and the performance of the two preceding stages dropped. The total expansion ratio of the first two turbines dropped from 3.2 to 2.77, and the maximum enthalpy drop was lower than 90% of the design value. If one continues to increase the reverse pressure, one only increases the load in the following stages without increasing the load in the preceding stages. This is not desirable in turbine design. The equation given in this paper can be used to find the ratio of passage area that will not cause choke to occur too early in the following stages under given conditions for the blade section angle and the Mach numbers for the various sections, thus avoiding undesirable results. In order to be able to quantitatively determine the extent of choke at the critical section and at the various other sections, we recommend the use of the concept of choke ratio and choke tolerance. Choke ratio is the ratio of the extent of choke of a certain blade row section to the critical value. The choke tolerance can be used to determine the flow condition that each blade row should be in. When it is required to have a large expansion ratio in the first stage, i.e., the first stage is to be highly transonic, then the following stage should have a large choke tolerance. Otherwise, choke will occur prematurely in the following stage and the first stage will not attain the desired expansion ratio. If, on the contrary, the first stage has a large choke ratio, then the load on the first stage will be too large, while that on the following stage will be too small. The efficiency of

the first stage will be low and the capability of the following stage will not be fully realized. Thus the choke tolerance has to be assigned in accordance with the requirement of each section so as to ensure proper matching of the stages.

3. Results and Analysis

By using the above equation in the computation for the transonic turbine operating under varied conditions, one can effectively analyze the stage matching of a multi-stage turbine. We carried out the computation for the performance of a multi-stage twin-shaft turbine. The results show that, when the stationary blade stagger angle of the first stage turbine is adjusted, the relation between the efficiency and relative choke ratio of the first stage is as shown in Figure 1. This relation very closely approximates a straight line. One can see that the efficiency of the turbine stage increases as the relative choke ratio approaches 1. If, on the other hand, the stationary blade stagger angle of the second stage is adjusted, the results are as shown in Figure 2. When the stagger angle is increased, the mass flow is reduced, while when the stagger angle is decreased, the mass flow remains the same. This indicates that, when the stationary blade stagger angle of the second stage is reduced, the critical section is still in the first stage. The mass flow being restricted by the critical section in the first stage, stays unchanged. When the stationary blade stagger angle of the second stage is increased, the critical section shifts can be conveniently described and determined in terms of the relative choke ratio. It is clear from Figure 2 that the position of the critical section changes as the stagger angle of the second stage is varied. When this stagger angle is increased, the corresponding relative choke ratio also increases gradually. When the stagger angle becomes larger than 1° , the critical section is shifted to the second stage. As for stage matching of a multi-stage turbine,

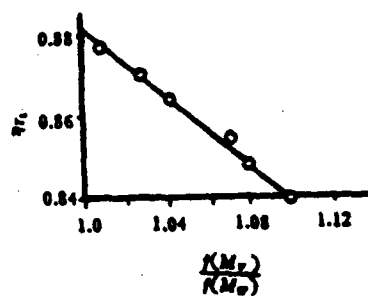


Figure 1. Efficiency vs. choke ratio for the first stage.

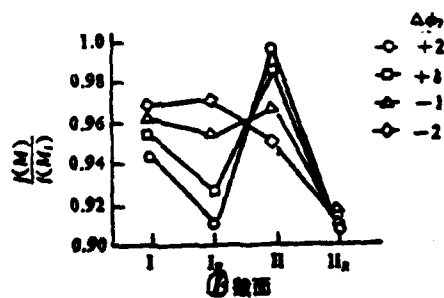


Figure 2. Relative choke ratio vs. $\Delta\phi_2$.
Key: 1) section.

the variation of relative choke ratios of the various blade rows can be seen in Figure 2, and the position of the critical section can be easily determined. It is also very convenient and effective to use the relative choke ratio to obtain the optimal arrangement of the blade rows. When the relative choke ratios of the various stages are not distributed properly, e.g., the value for the second stage is larger than that for the first stage, then the critical section will be located in the second stage and the enthalpy drop (or expansion ratio) of the first stage will be severely restricted. In our example, a mere increase of 2° in the second stage blade stagger angle caused the first stage enthalpy drop to decrease over 20%. This shows that the correct positioning of the critical section is a crucial factor in the stage matching problem. From our computation and analysis, we have arrived at the following two conclusions.

(1) There is always an optimal stage matching for a multi-stage turbine corresponding to different design conditions. From the above discussion, we see that the single stage turbine has the highest efficiency when the relative choke ratio of the stationary blade row and the rotating blade row approaches 1. (The blade profile is assumed to be the same for the stationary and the rotating blades.)

(2) The choke ratio and choke tolerance are useful parameters in evaluating the flow and choke conditions for each blade row. These parameters are also useful in determining the performance of each section and the position of the critical section.

/162

(3) To obtain the best possible performance for each stage, critical section should be located at the stationary blade row of the first stage. This point is especially important for a turbine with a large load. Otherwise, the load in the first stage may be too small, and the number of stages has to be increased.

(4) It is recommended to use the equations given in this paper in conjunction with the computer program for the computation of the operation of the transonic turbine under varied conditions in the solution of the stage matching problem.

INVESTIGATION OF THE ROTOR WAKE IN A SINGLE
STAGE AXIAL FLOW COMPRESSOR*

Chang Wei-te, Lin Ch'i hsun
(Northwestern Polytechnical University)

ABSTRACT

We find that the development of the rotor wake is similar for both rotating stall and surge. So it proves that the rotor wake is the origin of the unsteady operation of compressor and the unsteady form only depends on the acoustic performance of the compressor system.

/163

The parameter of the rotor wake can be used to calculate the loss of the cascade.

The rotor wake is one of the origins of the unsteady operation of the compressor and fundamentally determines the loss in the blade cascade.

We measured the velocity wake at the rotational speeds of 5000, 8232, 10,765 and 12,700 rpm by means of the 55R34 bend-head hot film and the 55M01 hot wire anemometer placed at $0.2b$ from the trailing edge of the blades of a subsonic single stage compressor. The hot wire signals were fed into an oscilloscope with memory and photographed. Figures 1 and 2 show the wave forms for the wakes under the various flow regulating valves, at the rotational speeds of 5000 and 12,700 rpm (the valves were adjusted from 50 to 69, the flow creased, and the corresponding mass flow coefficient \bar{C}_{1a} decreased from 0.6 to 0.4). The experiment shows that for rotational speeds below 10,760 rpm rotating stall preceded surge, while for higher rotational speeds, surge occurred directly. In either case, the variation in the wake wave form is fundamentally the same. For $\bar{C}_{1a} = 0.6$, the wakes of the pressure side and the suction side are basically

* This paper was read during the 3rd National Meeting of the Engineering Thermophysics Conference held in Kueilin during April 1980.

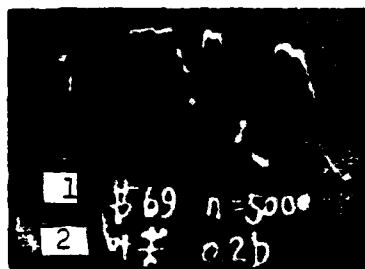
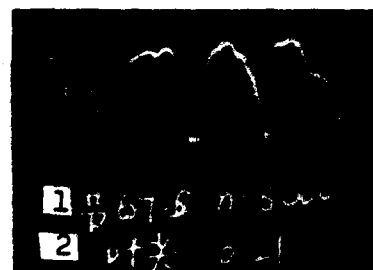
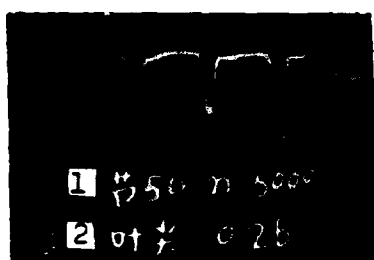


Figure 1. Changes in the wake during the transition from steady operation to rotating stall at low rotational speeds ($n = 5000$ rpm)
1--flow regulating valve; 2--blade tip

symmetrical. The relative thickness in the wake region δ (which is the ratio of the width of the wake to the cascade spacing) is small, only about 0.3. With the decrease of the mass flow, the wake widens and when $\overline{C}_{1a} = 0.4$, $\delta \approx 1$, and the main flow region almost completely disappears. This variation can be clearly seen in the examples given in Figures 1 and 2. Repeated tests show that the repeatability is high. This proves that the rotor wake is one of the causes of unsteady operation, as it directly leads to rotating stall and surge. Whether rotating stall or surge ensues depends on the acoustic performance of the compressor. A criterion B has been given by Greitzer [1]; when $B > 0.8$, surge will occur, and when $B < 0.8$, rotating stall will take place. Using the dimensions of our compressor, we found $B = 0.8$ for $n = 10765$ rpm. Therefore, our experimental results agree basically with his conclusion.

The wake essentially determines the loss in the rotating blade cascade. We therefore attempt to determine this loss by means of the

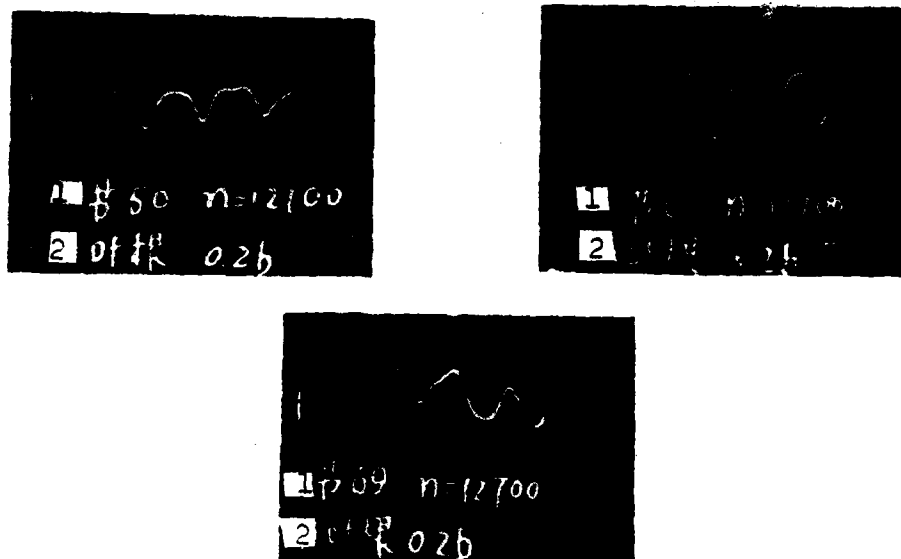


Figure 2. Changes in the wake when surge was directly induced at high rotational speed ($n = 12700$ rpm)

1--flow regulating valve; 2--blade root

wake parameters. To simplify the process, we assume that the wake is symmetrical and the velocity distribution is linear in the wake region as shown in Figure 3. We also assume that: 1) the static pressure is the same in the main flow region and the wake region; 2) the flow is incompressible; 3) there is no loss in the total pressure in the main flow region; 4) the flow exit angle β_2 is the same in the main flow region and the wake region. Thus, the following relation can be derived for the loss coefficient $\bar{\omega}$ (the derivation is omitted here):

$$\bar{\omega} = \frac{\cos^2 \beta_1}{\cos^2 \beta_2} \left[\left(1 + \frac{\Delta U}{2U_{2m}} \delta \right)^2 - 1 \right] \quad (1)$$

In the above equation, β_1 is the flow angle at the inlet; U_{2m} is the average flow velocity at the exit, where $U_{2m} = U_{2m1} - 0.5(\Delta U \cdot \delta)$. Actually, equation (1) is a special case of Lieblein's [2] equation for this simplified wave form. Figure 4 shows the variation with \bar{C}_{1a} of $\bar{\omega}$ obtained from the wake data taken at 0.2b behind the trailing edge of the blade tip for $n = 10760$ rpm. We have also given the results obtained for the actual wave form using the Lieblein equation and the results obtained by means of the steady-state probes. It can

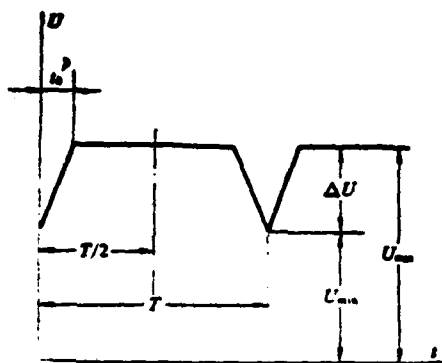


Figure 3. Simplified diagram of the wake wave form

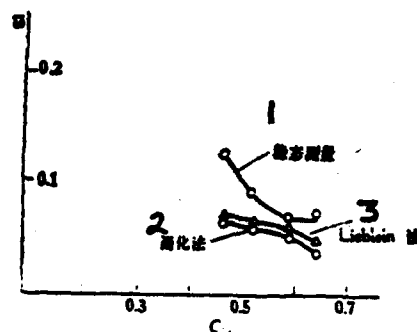


Figure 4. Relation between cascade loss coefficient $\bar{\omega}$ and mass flow coefficient \bar{C}_{la}

1--steady-state measurement;
2--simplified method;
3--Lieblein method

be seen from Figure 4 that our results are fairly close to those obtained using Lieblein's method. On the whole, the results of all three methods are on the same order of magnitude. The values from steady-state measurements are on the high side when \bar{C}_{la} is small. This may be attributed to the effects of three-dimensional flow.

This is a first attempt at determining the loss in the rotating blade cascade by means of a dynamic scheme. It is, however, apparent that this approach is feasible. The crux lies in precisely calibrating the dynamic probes, which we have not yet been able to do. We will be directing our efforts toward the solution of this calibration problem. Furthermore, we will use a computer to process the data. It will thus be totally possible to use the dynamic method to determine the loss in the rotating blade cascade or the primary blade cascade.

Other comrades who participated in this work include Liu Chih-wei, Liu Chia-fong, Liu Chao-jen, Chang Ch'ang-sheng, Shih Ching-hsun and Chang Tao-sheng.

REFERENCES

- [1] Greitzer, E. M: Surge of Rotating Stall in Axial Flow Compressor, *Trans. of ASME, Series A*, 98, 2, (April, 1976), 190-217.
- [2] Lieblein, S. and Roudebush, W. H.: Theoretical Loss Relations For Low-Speed Two-Dimensional-Cascade Flow, *NACA TN 3082* (April, 1956).

ADDENDUM

Chang Ch'un-lin: The Application of the Equations for Integration by Approximation in Tests and Computations on Bladed Machines", Naval Vessel Turbines and Steam Engines, No. 1, 1976.

The above should be added to the references given at the end of the article: Tests and Analysis of Parameters along the Entire Flow Path in a Turbojet Engine, p. 204, No. 2, 1980, in this publication.

The former article is the source of Chebychev selection of points for integration by approximation.

THERMAL CONDUCTIVITY MEASUREMENT OF MATERIALS DURING ABLATION--A TREATMENT ON THE MOVING BOUNDARY PROBLEM*

Chou Pen-lien, Wei Chen, Lin Chun-heng
(Institute of Metal Research, Academia Sinica)

ABSTRACT

/166

It is necessary to measure the continuous variation of a thermal conductivity of coatings due to structural changes during ablation, so tests have been carried out under the conditions simulating the practical operation on specimens similar to actual components. The thermal diffusivity α and thermal conductivity k have been calculated in this paper from the temperature rise curves of the inner and outer surfaces of specimen and the change in dimensions during ablation by arc plasma. It is suggested in this paper that the moving boundary of constant temperature model can be substituted by the fixed boundary of varying temperature model to treat the case with ablation; in the case without ablation, the unknown quantities q_c (the heat flow) and k can be cancelled at first by calculating the ratio of temperature increases of the inner and outer surfaces of specimen, and then k and q_c can be calculated as the value of α is obtained.

I. FOREWORD

Structural changes occur continuously in coatings on metals during the process of ablation. Therefore, in measuring the continuously varying thermal conductivity of the coating, one should use specimens similar to the actual components and carry out the tests under

*This paper was read during the 3rd National Meeting of the Engineering Thermophysics Conference held in Kueilin during April 1980.

conditions that are very similar to those of the actual operation.

The temperature rise curves of the inner and outer surfaces of the coating and the change in dimensions during ablation can be obtained from arc plasma experiments. Based on this, we have calculated the thermal diffusivity of the coating material, and obtained the thermal conductivity of the coating from the values of specific heat and density. The specimen was prepared by taking a niobium alloy tube 20 mm in diameter, 100 mm in length and with wall thickness 3.5 mm, and spraying on it a 0.3 mm thick coating of silicon oxide and magnesium oxide and a 0.7 mm thick coating of aluminum oxide. Then the outermost layer was added which consisted of a 4 mm thick wrapping made of aluminum phosphate bonded to a quartz belt. For details, see [1].

II. EXPERIMENTAL DATA AND METHOD OF COMPUTATION

The experiments were divided into two groups. In the first group, the heat flow was strong. The surface temperature steadied in a short time without much fluctuation, but the surface was continually ablated. In the second group, the heat flow was weaker and the temperature rose at a slower rate. We applied the moving boundary of constant temperature model to the former and the constant heat flow boundary model to the latter.

1. Moving boundary of constant temperature

The surface of the three samples in Figure 1 reached a temperature above 2400°C in a very short time (14.1 sec). Fluctuations generally stayed within 4%, with a maximum of 7.5%. Hence, one can regard the outer surface of the sample as the constant temperature boundary. The quartz belt on the outer layer of the sample reached the boiling point of 2950°C [2] in a short time in the plasma flame. While the coating became thinner because of ablation, the surface temperature remained the same, close to the boiling point, which could have been lowered a little by the presence of the bonding material.

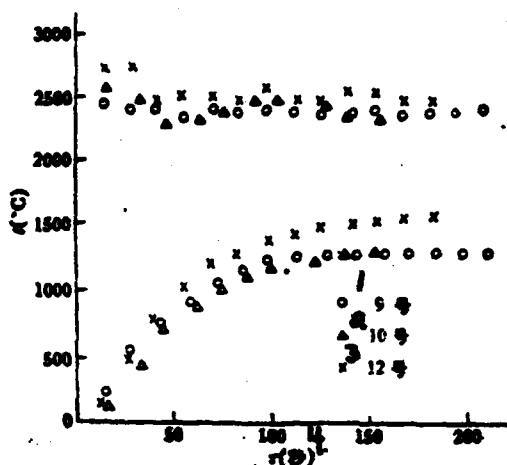


Figure 1. Temperature rise on the inner and outer surfaces of the sample (under the condition of moving boundary of constant temperature)
1--no. 9; 2--no. 10; 3--no. 12; 4--sec.

The sample was rotated about a vertical axis. In the isothermal region, the radial heat loss was very small. The tube was stopped with quartz fabric so as to prevent heat loss from convection. Because the sample was rotating, it was heated uniformly and, therefore, the inner surface also had approximately a uniform temperature. Owing to the balance of radiation, heat loss was very small and the inner surface could be considered as an adiabatic boundary. /167

As the coating was a thin layer, it was uniformly heated. Therefore, the direction of heat flow was perpendicular to the inner and outer surfaces of the coating in the isothermal region and the problem reduced to that of one-dimensional heat conduction in a large slab. Taking the x-axis to be along the direction perpendicular to the surface, and the origin to be on the inner wall, we have

$$\frac{\partial t(x, \tau)}{\partial \tau} = a \frac{\partial^2 t(x, \tau)}{\partial x^2}, (\tau > 0, 0 < x < R_1) \quad (1)$$

$$R_i = R(\tau_i) \quad (2)$$

$$\begin{cases} t(x, \tau_i) = f_i(x), (i = 0, 1, 2, \dots) [i = 0, f_0(x) = t_0] \\ t(R_i, \tau) = t_c = \text{constant} \end{cases} \quad (3)$$

$$\begin{cases} \frac{\partial t(0, \tau)}{\partial x} = 0. \end{cases} \quad (4)$$

In the above equations, t is temperature; t_0 is initial temperature; $f_1(x)$ is the distribution of initial temperature; t_c is the constant temperature of the outer surface; τ is time; R_1 is the thickness of the coating which became smaller and smaller during the ablation; α is the thermal diffusivity.

This problem is one of thermal conduction in a large slab with boundary conditions of the first type [3] for which a solution exists. Note, however, that the problem in [3] is one with a stationary boundary, while that at hand is one of a moving boundary. In general, the solution can be found by the method of successive substitution.

Given the initial temperature of the coating $t(x, 0) = f_1(x)$, the solution for equations (1)-(4) is [3]:

$$\begin{aligned} t(x, \tau) - t_c = & \sum_{n=0}^{\infty} \cos \frac{(2n+1)\pi x}{2R_i} \cdot e^{-\frac{(2n+1)^2 \pi^2 \tau}{4R_i^2}} \\ & \cdot \frac{2}{R} \int_0^R \{f_1(x') - t_c\} \cdot \cos \frac{(2n+1)\pi x'}{2R_i} dx' \end{aligned} \quad (5)$$

First, let $R = R_0$, and find the $t(x, \tau_1) = f_1(x)$ at $\tau = \tau_1$, to be used as the temperature distribution for $R = R_1$. Substituting this into equation (5) gives the $t(x, \tau_2) = f_2(x)$ at $\tau = \tau_2$, and so on. As the series converges rather slowly, the calculation is tedious even with the help of a calculator. In the following we attempt to treat this problem using a different approach. The main idea is to use the fixed boundary of a varying temperature model instead of the moving boundary of constant temperature model in studying the temperature variation inside an object as related to the thermal properties of that object.

Suppose there is a flat slab (Figure 2) of thickness R_0 . Let the initial temperature be $f(x)$. Assume there is no heat flow at $x = 0$, and the temperature at $x = R_0$ is $\phi(\tau)$. Then, the temperature of point x at time τ will be [4]:

$$t(x, \tau) = \frac{2}{R_0} \sum_{n=0}^{\infty} e^{-\alpha(m+1)^2 \tau / R_0^2} \cdot \cos \frac{(2n+1)\pi x}{2R_0} \left\{ \frac{(2n+1)\pi (-1)^n}{2R_0} \cdot \int_0^{\tau} e^{\alpha(m+1)^2 \tau' / R_0^2} \cdot \phi(\tau') d\tau' + \int_0^{R_0} f(x') \cos \frac{(2n+1)\pi x'}{2R_0} dx' \right\} \quad (6)$$

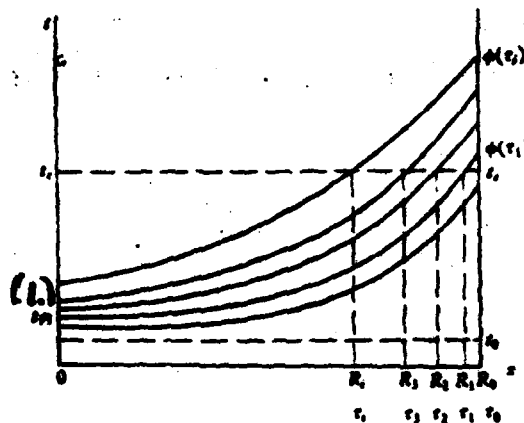


Figure 2. Schematic diagram of the moving boundary
1--inner

From the mean value theorem of integration (letting β and γ be two parameters between 0 and 1), the above equation can be written as:

$$\begin{aligned} t(x, \tau) &= \frac{2}{R_0} \sum_{n=0}^{\infty} e^{-\alpha(m+1)^2 \tau / R_0^2} \cdot \cos \frac{(2n+1)\pi x}{2R_0} \left\{ \frac{(2n+1)\pi (-1)^n}{2R_0} \cdot \phi(\beta\tau) \int_0^{\tau} e^{\alpha(m+1)^2 \tau' / R_0^2} \cdot d\tau' + f(\gamma R_0) \int_0^{R_0} \cos \frac{(2n+1)\pi x'}{2R_0} dx' \right\} \\ &= \frac{4}{\pi} \sum_{n=0}^{\infty} \left[e^{-\alpha(m+1)^2 \tau / R_0^2} \cdot e^{\alpha(m+1)^2 \tau / R_0^2} \cdot \cos \frac{(2n+1)\pi x}{2R_0} \cdot \frac{(-1)^n}{2n+1} \phi(\beta\tau) - e^{-\alpha(m+1)^2 \tau / R_0^2} \cdot \cos \frac{(2n+1)\pi x}{2R_0} \cdot \frac{(-1)^n}{2n+1} \cdot \{ \phi(\beta\tau) - f(\gamma R_0) \} \right] \end{aligned}$$

$$\begin{aligned}
&= \frac{4}{\pi} \phi(\beta\tau) \sum_{n=0}^{\infty} \frac{(-1)^n}{2n+1} \cdot \cos \frac{(2n+1)\pi x}{2R_0} + \frac{4}{\pi} \{f(\gamma R_0) - \phi(\beta\tau)\} \\
&\quad \cdot \sum_{n=0}^{\infty} \frac{(-1)^n}{2n+1} e^{-\alpha(m+1)^2 \tau^2 / 4R_0^2} \cdot \cos \frac{(2n+1)\pi x}{2R_0} \\
&= \phi(\beta\tau) + \frac{4}{\pi} \{f(\gamma R_0) - \phi(\beta\tau)\} \cdot \sum_{n=0}^{\infty} \frac{(-1)^n}{2n+1} e^{-\alpha(m+1)^2 \tau^2 / 4R_0^2} \\
&\quad \cdot \cos \frac{(2n+1)\pi x}{2R_0}, \text{ which can be expressed as}
\end{aligned}$$

$$\frac{t(x, \tau) - \phi(\beta\tau)}{f(\gamma R_0) - \phi(\beta\tau)} = \frac{4}{\pi} \sum_{n=0}^{\infty} \frac{(-1)^n}{2n+1} e^{-\alpha(m+1)^2 \tau^2 / 4R_0^2} \cdot \cos \frac{(2n+1)\pi x}{2R_0} \quad (7)$$

/169

(1) When the initial temperature is t_0 (i.e., $f(x) = f(\gamma R_0) = t_0$), and the temperature remains the same on the right surface, at t_0 (i.e., $\phi(\tau) = \phi(\beta\tau) = t_0$), equation (7) becomes

$$\frac{t(x, \tau) - t_0}{t_0 - t_0} = \frac{4}{\pi} \sum_{n=0}^{\infty} \frac{(-1)^n}{2n+1} e^{-\alpha(m+1)^2 \tau^2 / 4R_0^2} \cdot \cos \frac{(2n+1)\pi x}{2R_0} \quad (8)$$

This represents the condition of a stationary boundary at constant temperature [4].

(2) If at τ_{i-1} the boundary is at $x = R_{i-1}$, the temperature is t_0 , the internal temperature is $f_{i-1}(x)$, and at τ_i the temperature at any point in the slab is $t(x, \tau_i)$, then there exists a function $\phi(\tau)$ such that the following relation holds.

$$\frac{t(x, \tau_i) - t_0}{f_{i-1}(\gamma_{i-1} R_{i-1}) - t_0} = \frac{t(x, \tau_i) - \phi(\beta \tau_i)}{t_0 - \phi(\beta \tau_i)} \quad (9)$$

Similarly,

$$\frac{t(x, \tau_{i+1}) - t_0}{f_i(\gamma_i R_i) - t_0} = \frac{t(x, \tau_{i+1}) - \phi_{i+1}(\beta_{i+1} \tau_{i+1})}{t_0 - \phi_{i+1}(\beta_{i+1} \tau_{i+1})} \quad (10)$$

If ϕ_0, ϕ_{i+1} and ϕ_1, ϕ_2, \dots are functions of the same form, then the moving boundary of constant temperature model can be replaced by the stationary boundary of varying temperature model. The process

1) The Fourier expansion for the constant 1 in the open interval $(-R_0, R_0)$ [5]

$$1 = \frac{4}{\pi} \left(\sin \frac{\pi x}{2R_0} - \frac{1}{3} \cos \frac{3\pi x}{2R_0} + \frac{1}{5} \frac{5\pi x}{2R_0} - \dots \right)$$

of computation in evaluating thermophysical properties can thus be reduced to one of determining the parameters of $\phi(\tau)$ ¹⁾ using a finite number of values of R_i .

To simplify the computation, we have chosen for the boundary temperature rise function [4] the function $\phi(\tau) = (t_c - t_0)e^{\alpha\tau}$ which has a single parameter, and obtained

$$\frac{t(x, \tau) - t_c}{t_c - t_0} = e^{\alpha\tau} \frac{\cosh x(\nu/\alpha)^{1/2}}{\cosh R_0(\nu/\alpha)^{1/2}} - \frac{4}{\pi} \sum_{n=0}^{\infty} \frac{(-1)^n e^{-\alpha(n+1)^2 \tau / R_0^2}}{(2n+1) [1 + \{4\nu R_0^2 / (2n+1)^2 \alpha\}]} \cdot \cos \frac{(2n+1)\pi x}{2R_0} \quad (11)$$

When $\nu = 0$, equation (11) becomes equation (8).

Taking the data given in Figure 1 and using equations (5) and (8) to determine the α_0 and α_1 at $x = R_0$ and R_1 for each sample to be substituted into equation (11), one can find the individual parameters ν_1 . The temperature function is thus determined. If we let $x = 0$, the temperature of the inner wall is given by

$$\frac{t(0, \tau) - t_0}{t_c - t_0} = e^{\alpha\tau} \frac{1}{\cosh R_0(\nu/\alpha)^{1/2}} - \frac{4}{\pi} \sum_{n=0}^{\infty} \frac{(-1)^n e^{-\alpha(n+1)^2 \tau / R_0^2}}{(2n+1) [1 + \{4\nu R_0^2 / (2n+1)^2 \alpha\}]} \quad (12)$$

Substituting the data representing the variation with time of the temperature of the inner and outer walls, as given in Figure 1, into equations (11) and (12), one can obtain a series of values for α from which the average $\bar{\alpha}$ can be found. The corresponding temperature is

$$K(x, \tau) = \frac{1}{R_i} \int_0^{R_i} t(x, \tau) dx \quad (13)$$

The value of $\bar{\alpha}$ can then be used in $k = \alpha c_p \rho$, along with the specific heat c_p and density ρ to calculate the thermal conductivity k of the coating at \bar{t} .

¹⁾ For example, $\phi(\tau) = a_0 + a_1\tau + a_2\tau^2 + \dots + a_n\tau^n + \dots + a_m\tau^m$.

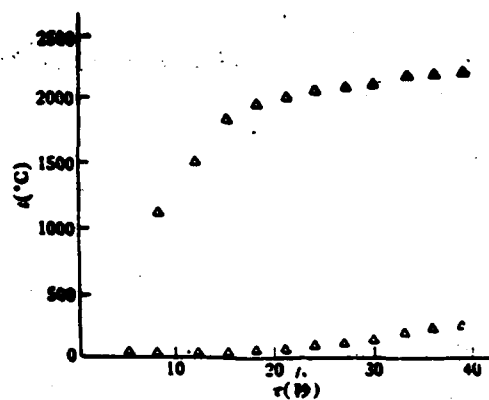


Figure 3. Temperature rise on the inner and outer surfaces of the sample (under the condition of constant heat flow boundary).

Key: 1. sec.

2. Constant heat flow boundary condition

/170

There was a temperature rise at both the inner and outer walls of the sample. Therefore, the boundary cannot be regarded as being at constant temperature. However, there was no ablation. The temperature of the plasma flame was above 6000 K, but the sample surface temperature did not exceed 2500 K. The ratio of the heat radiated is given by

$$\frac{H_{\text{sample}}}{H_{\text{plasma}}} = \frac{\sigma \cdot 2500^4}{\sigma \cdot 6000^4} = \frac{2.5^4}{6^4} \approx 3\%$$

Therefore, we can neglect the outward radiated heat flow. The inward radiated heat flow q_c is nearly constant. Other conditions are the same as given above. We have

$$\frac{\partial t(x, \tau)}{\partial \tau} = a \frac{\partial^2 t(x, \tau)}{\partial x^2}, \quad (\tau > 0, 0 < x < R) \quad (1')$$

$$t(x, 0) = t_0 \quad (2')$$

$$\left\{ \frac{-\partial t(R, \tau)}{\partial x} + \frac{q_c}{k} = 0 \right. \quad (3')$$

$$\left. \frac{\partial t(0, \tau)}{\partial x} = 0 \right\} \quad (4')$$

the solution of which is [3]

$$t(x, \tau) - t_0 = \frac{q_c}{k} \left[\frac{\alpha \tau}{R} - \frac{R^2 - 3x^2}{6R} + R \sum_{n=1}^{\infty} (-1)^{n+1} \frac{2}{\mu_n^2} \cos \mu_n \frac{x}{R} e^{-\mu_n^2 F_0} \right] \quad (14)$$

In the above equation, $\mu_n = n\pi$, $F_0 = \alpha \tau / R^2$ is the Fourier modulus.

We use the following method to overcome the difficulty of having q_c and k as unknowns. Let $x = R$. Since $(-1)^{n+1} \cos \mu_n = -1$, the temperature rise on the outer surface is

$$t_{\text{outer}} - t_0 = \frac{q_c R}{k} \left[F_0 + \frac{1}{3} - \sum_{n=1}^{\infty} \frac{2}{\mu_n^2} e^{-\mu_n^2 F_0} \right] \quad (15)$$

Let $x = 0$. The temperature rise on the inner surface is

$$t_{\text{inner}} - t_0 = \frac{q_c R}{k} \left[F_0 - \frac{1}{6} + \sum_{n=1}^{\infty} (-1)^{n+1} \frac{2}{\mu_n^2} e^{-\mu_n^2 F_0} \right] \quad (16)$$

The relative temperature rise ratio for the inner and outer surfaces is

$$\frac{\theta_{\text{outer}}}{\theta_{\text{inner}}} = \frac{t_{\text{outer}} - t_0}{t_{\text{inner}} - t_0} = \frac{F_0 + \frac{1}{3} - \sum_{n=1}^{\infty} \frac{2}{\mu_n^2} \cdot e^{-\mu_n^2 F_0}}{F_0 + \frac{1}{6} + \sum_{n=1}^{\infty} (-1)^{n+1} \frac{2}{\mu_n^2} e^{-\mu_n^2 F_0}} = \phi(F_0) \quad (17) \quad /171$$

where the unknown quantities q_c and k have been cancelled.

The relative temperature rise ratio $\theta_{\text{outer}}/\theta_{\text{inner}}$ is a function of F_0 only. The solution can be found by making some changes in the diagram given on page 162 of [3]. In the diagram, F_0 is the abscissa and θ/K_1 is the ordinate, where K_1 is the Chebychev modulus. $\theta_{\text{outer}}/K_1$ and $\theta_{\text{inner}}/K_1$ are separately given in the diagram. Take the ratio of these values for a given F_0 and cancel the K_1 , and the solution is readily obtained. The relation of the ratios thus obtained to F_0 can be tabulated (omitted here).

The value of $\theta_{\text{outer}}/\theta_{\text{inner}}$ can be found from Figure 3. The corresponding value of F_0 can be found from the table. Thus, α and k can be obtained from the definition of F_0 , $\alpha = F_0 R^2/\tau$.

The data in Figure 3 can also be used directly in equations (11) and (12), treating the problem as one of stationary boundary of varying temperature.

3. Results of computation

Figure 4 gives the values of α calculated for the two groups of samples under their respective conditions and the values of k obtained from $\bar{\alpha}$. There is a fairly good continuity of the results obtained using the two methods. As the coating consists of three layers of different materials and the samples do not have exactly the same composition, the deviation of the two high temperature data points for sample no. 12 from the curves for the other two samples is understandable.

In computing for the thermal conductivity, we have introduced the specific heat and density of each layer in a weighted relation like the following:

$$\rho c_p = (a_1 \rho_1 c_{p1} + a_2 \rho_2 c_{p2} + a_3 \rho_3 c_{p3}) / (a_1 + a_2 + a_3) \quad (18)$$

where a_1 , a_2 and a_3 are the thicknesses of the layers of coating, which become variables in the case of ablation. ρ_1 , c_{p1} , etc., are the density and specific heat of each layer.

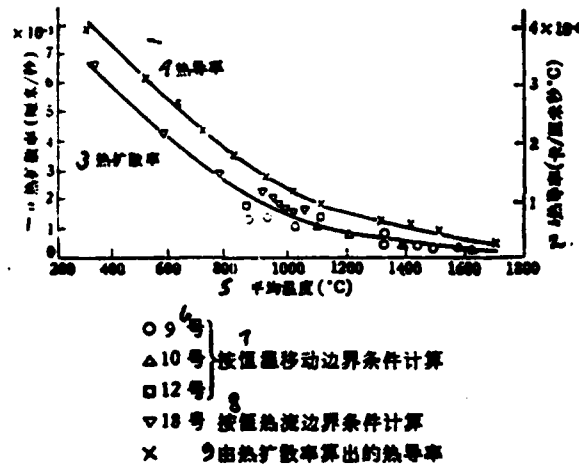


Figure 4. Relation between α , k and temperature for a high temperature resistant thermally insulating composite coating (obtained from the temperature rise curve from thermally insulated ablation experiment).

1--thermal diffusivity (cm/sec); 2--thermal conductivity (cal/cm·sec·°C); 3--thermal diffusivity; 4--thermal conductivity; 5--average temperature (°C); 6--number; 7--as obtained under the condition of moving boundary of constant temperature; 8--as obtained under the condition of constant heat flow boundary; 9--thermal conductivity obtained from thermal diffusivity

III. DISCUSSION

1. As ablation is accompanied by melting and vaporization, the measured values are the effective thermal conductivities. /17

2. After α and k are found, q_c can be calculated using equation (15) or (16).

3. The thermal conductivity during ablation has been obtained in this paper by solving for it under given boundary conditions. This method can also be applied to problems under different experimental conditions.

REFERENCES

- [1] Institute of Metal Research: High Temperature Experiments using low Power Arc Plasma, May, 1974.
- [2] Campbell, I. E. High Temperature Technology (John Wiley & Sons, 1956), translated by Kao Yang et al, K'e Hsueh Publishing House, 1961, 26.
- [3] 雷柯夫, A. B. Theory of Thermal Conduction (1952), translated by Ch'iu Lieh'chun and Ting Lu'te, Kao Teng Chiao Yu Publishing House, p. 95, p. 155.
- [4] Carslaw, H. S. and Jaeger, J. C. Conduction of Heat in Solids, 2nd ed., p. 104, p. 100.
- [5] Fan Ying-Ch'uan et al: Lectures on Advanced Mathematics. Jen Min Chiao Yu Publishing House, book 2, p. 69.

A METHOD FOR MEASURING MULTIPLE THERMALPHYSICAL
PROPERTIES OF METALLIC MATERIALS AT HIGH TEMPERATURE*

/173

Yao Lung-ch'in, He Lu-ping, Hao-Yu-ts'ai, Kuo-I'ling,
and Wang Hui-ying
(General Research Institute for Nonferrous Metals of
MMI)

ABSTRACT

In this paper a method for measuring multiple thermophysical properties of metals and alloys at high temperature was introduced; a new experimental apparatus has been developed; electrical resistivity, thermal conductivity, coefficient of expansion, hemispherical total emittance, normal spectral emittance (0.65μ) have been measured. The results are found to be in accord with the TPRC data. The probability of replacing a thin tube method with rod specimen for metallic materials to measure spectral emittance has been discussed.

1. Introduction

There are obvious advantages for measuring many thermophysical properties all at once in a single experiment. We have, therefore, designed and developed a general purpose apparatus that can be used to measure multiple thermophysical properties of metals at high temperatures. These properties include spectral emittance at 0.65μ , hemispherical total emittance, electrical conductance, thermal conductance, coefficient of linear expansion and melting point.

2. Principle of method

(1) Determination of spectral emittance ϵ_λ at 0.65μ .

* This paper was read during the 3rd National Meeting of the Engineering Thermophysics Conference held in Kueilin during April 1980.

Wien's law is given by $\ln \epsilon_\lambda = \frac{C_2}{\lambda} \left(\frac{1}{T} - \frac{1}{T'} \right)$. Therefore, by drilling a hole in the sample in the region of uniform temperature and measuring the temperatures at the bottom and at the rim of the hole by means of an optical pyrometer, the spectral emittance can be found from Wien's formula by inserting these temperature values into the formula. The hole is assumed to be a black body. Two corrections need to be made in this measurement: (a) for the error in temperature arising from the difference between the bottom of the hole and a true black body; (b) for the emission of heat from the isothermal region, which results in a temperature difference between the center and the surface of the sample. Analyses [1],[2] show that the error in temperature arising from the first factor is $\Delta T = \frac{C_2 T'}{C_2 + \lambda T' \ln \epsilon_{0\lambda}} - T'$, where T' is the temperature of the bottom of the hole as measured by the optical pyrometer, and $\epsilon_{0\lambda}$ is the absorptivity of the bottom of the hole. The error in temperature from the second factor is $\xi = \frac{0.239 VI}{4\pi LK} \left(1 - \frac{r^2}{R^2} \right)$,

where V , L and I are the voltage drop, length and current intensity, respectively, of the isothermal section of the sample. K is the heat conduction coefficient of the sample, r is the distance from the center of the sample to the bottom of the hole and R is the radius of the sample.

(2) Determination of resistivity ρ .

From Ohm's law, we have in the isothermal region of the sample

$$\rho = \frac{\pi R^2 V}{IL}$$

(3) Determination of hemispherical total emittance ϵ_{ht} .

From the Stefan-Boltzman law, in the isothermal region of the sample, $\epsilon_{ht} = \frac{IV}{A\sigma(T^4 - T_0^4)}$, where A is the surface area of the isothermal region; T and T_0 are the temperature of the sample and the water-cooled vacuum jacket, (K) respectively; and σ is the Stefan-Boltzman constant.

(4) Determination of the average expansion coefficient $\bar{\alpha}$.

From definition $\bar{\alpha} = \frac{L_T - L_0}{L_0 \cdot \Delta T}$, where L_T is the length of the isothermal region (at temperature T), L_0 is the length at room temperature, and ΔT is the difference between T and room temperature.

(5) Determination of thermal conductivity K.

From the method of using a long and a short sample to determine thermal conductivity [3], we have $K = \frac{S(I_2 - I_1)}{2S\beta}$, where I_2 and I_1 are the current intensities of the long and short samples, respectively; S is the cross-sectional area of the sample, and β is the slope of the temperature distribution curve in the vicinity of the center of the short sample.

/174

(6) Determination of the melting point.

The melting point can be determined by gradually heating the sample until it melts, observing the temperature of the bottom of the small hole, and making corrections on absorptivity.

3. Experimental set up and measurements

The experimental set up is an apparatus that we have put together for measuring multiple thermophysical properties. A special feature of the apparatus is the vacuum sealed movable electrodes, the distance between which can be adjusted according to sample length. The window for temperature measurement is made up of a pile (8 pieces) of quartz glass plates. When one of the glass plates is contaminated by evaporated metal, it can be removed without disturbing the vacuum. The quantities to be measured include: V--the voltage drop in the measured isothermal section of the sample, I--the current intensity in the sample, T--the temperature of the sample and L_T --the length of the measured isothermal section at temperature T, as determined using the optical pyrometer.

4. Samples

The samples were two industrial grade tungsten rods of length 200 mm and diameters $\phi 3$ and $\phi 5$ (mm). After buffing, the rods were annealed for a half-hour at 2000°C in vacuum. The $\phi 5$ sample was used in the determination of ϵ_{λ} and melting point. The other quantities were obtained from measurements performed on the other sample. The short sample needed in the determination of thermal conductivity was taken from the long sample.

5. Experimental results and discussion

The results of the measurements are shown in Figure 1. The curves in the diagram have been obtained by smoothing experimental data given in the references. All the experimental data obtained in this work have been dotted on the diagram. Using curve-fitting technique, the following empirical relations have been obtained for the various quantities:

$$\begin{aligned}\epsilon_{\lambda, \text{max}} &= 0.468755 + 1.59881 \times 10^{-4}T - 9.40576 \times 10^{-9}T^2 \\ \alpha &= (8.01275 \times 10^{-3} + 2.62027 \times 10^{-4}T - 3.13408 \times 10^{-8}T^2) \text{ degree}^{-1} \\ \rho &= (5.42532 + 8.32293 \times 10^{-3}T + 1.343 \times 10^{-5}T^2 - 2.2128 \times 10^{-9}T^3)(10^{-4}) \\ \epsilon_{\lambda} &= 0.61505 - 7.38875 \times 10^{-4}T + 3.93301 \times 10^{-7}T^2 - 5.88482 \times 10^{-10}T^3 \\ k &= (-0.799757 + 0.001515T - 7.25901 \times 10^{-7}T^2 + 1.16555 \times 10^{-10}T^3) \\ &\quad (\text{cal/cm} \cdot \text{degree} \cdot \text{sec})\end{aligned}$$

We made several measurements on the melting point of the high-melting point materials T_aC , H_fC and W. The variance was $\pm 30^\circ C$, approximately.

ξ and ΔT have opposite effects on the spectral emittance ϵ_{λ} . As these effects counteract each other, one can use the method of drilling a hole in a solid rod in the measurement of ϵ_{λ} of metallic materials with high thermal conductivity, instead of the thin wall method suggested by A. G. Worthing. The difference in the results obtained by the two methods is not large.

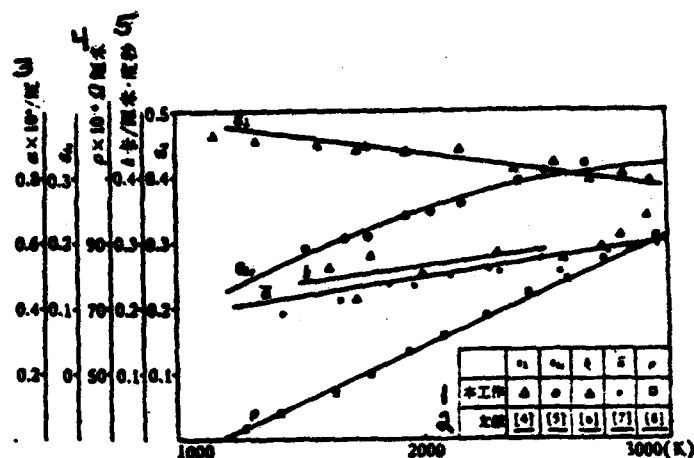


Figure 1. Relation between temperature and $\epsilon_{0.100}$, $\epsilon_{0.20}$, ϵ , ρ and k of W.

1--this work; 2--references; 3--degree; 4--cm; 5--cal/cm·degree·sec

REFERENCES

- [1] Chou Pen-lien et al: Determination of Thermal Conductivity, Resistivity and Emissivity of Graphite at High temperatures (1000-2700°C), Collection of Reports of the Annual Meeting of the National Test Stations (Book of Physical Properties), New Technologies Division, Academia Sinica, 1963, 13-24.
- [2] He Lu-ping: Method for Computing the Absorptivity of an Artificial Black Body, Rare Metals, 5, 1980, 63-68.
- [3] В. В. Лебедев: Определение коэффициента теплопроводности металлов в области высоких температур, ФММ, Том 10, 2, (1969), 187-190.
- [4] Y. S. Toulouhian: Thermal Radiative Properties-Metallic Elements and Alloys, IFI/PLENVM, New York, (1970), 791.
- [5] same as [4], 782.
- [6] Y. S. Toulouhian: Thermal Conductivity-Metallic Elements and Alloys, IFI/PLENVM, New York (1970), 782.
- [7] Y. S. Touloukian: Thermalphysical Properties of High Temperature Solid Materials, IFI/PLENVM, New York, (1968), 1029.
- [8] same as [6], 416.